Supporting Information

Engineering Pore Nanospaces through Introducing Aromatic Effect in UiO-66 for Efficient Light Hydrocarbons Separation

Liang Zhang, Xiao-Hong Xiong, Liu-Li Meng, Lu-Zhu Qin, Cheng-Xia Chen, Zhang-Wen Wei* and Cheng-Yong Su*

MOE Laboratory of Bioinorganic and Synthetic Chemistry, Lehn Institute of Functional Materials, School of Chemistry, Sun Yat-Sen University, Guangzhou 510275, China.
E-mail: weizhw3@mail.sysu.edu.cn.
cesscy@mail.sysu.edu.cn

Table of Contents

S1. Materials and Instrumentation

All reagents and solvents were obtained from commercial sources and used without further purification. Powder X-ray diffraction (PXRD) were recorded ranging from 2 º to 50 º at room temperature on a RigakuSmartLab diffractometer (Bragg-Brentano geometry, Cu Kα1 radiation, λ = 1.54056 Å) at 40 kV and 15 mA. Thermogravimetric analysis (TGA) was performed on a NETZSCH TG209 system in nitrogen and under 1 atm of pressure at a heating rate of 10 °C min^{-1}. N_2 adsorption isotherms for pressures in the range of 0-1.0 bar were collected by a volumetric method using a quantachrome autosorb IQ3 gas adsorption analyzer. The samples were vacuumed at 100 ºC for 12 h before the sorption examination. Gas adsorption isotherms were measured on a quantachrome Autosorb-iQ2-MP gas adsorption analyzer. The breakthrough curves were collected by a home-made instrument using a gas chromatography (FL-9790 plus) as detector.

S2. Powder X-Ray Diffraction

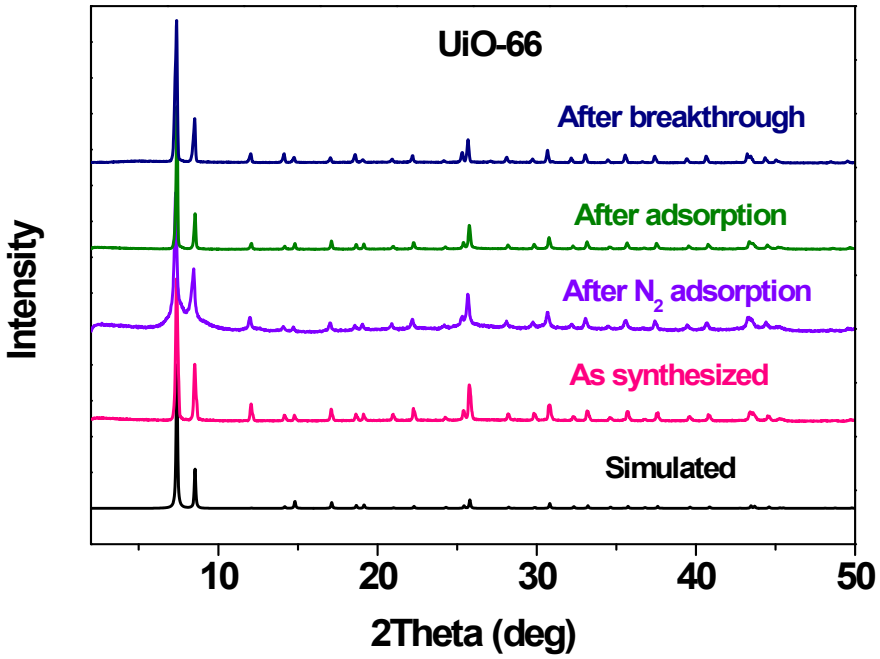

Figure S1. The simulated and experimental PXRD patterns of UiO-66.

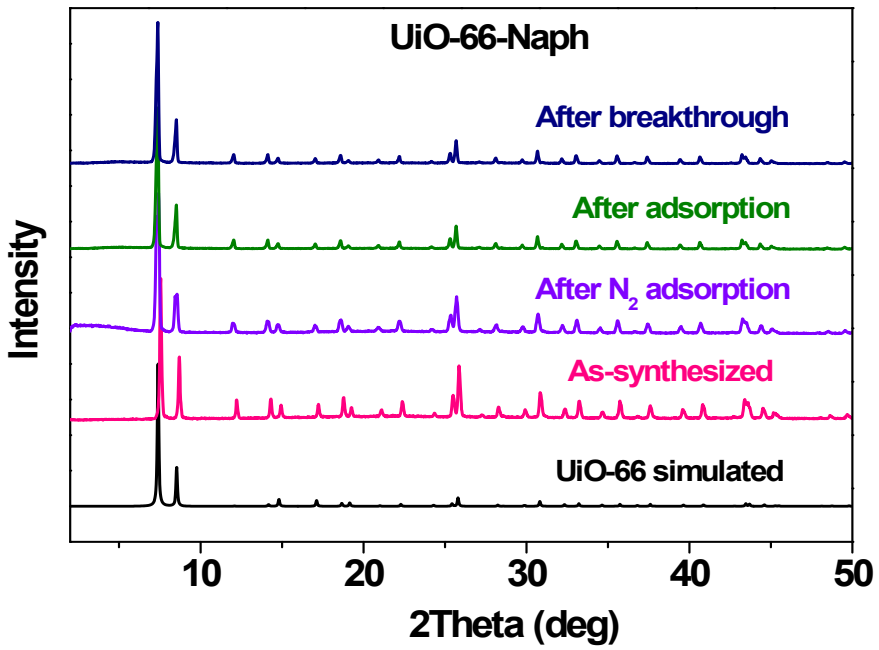

Figure S2. The simulated and experimental PXRD patterns of UiO-66-Naph.

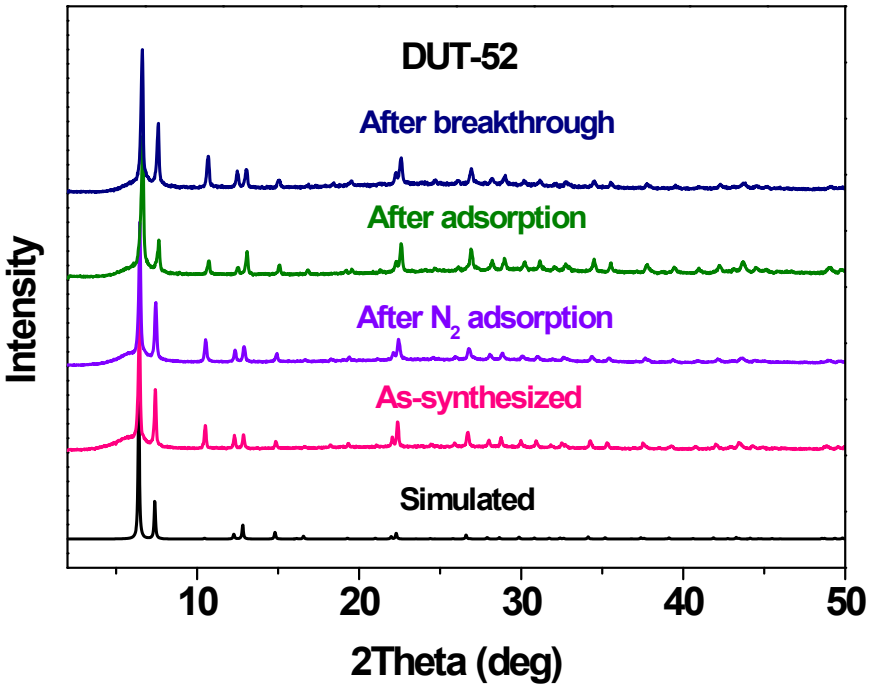

Figure S3. The simulated and experimental PXRD patterns of DUT-52.

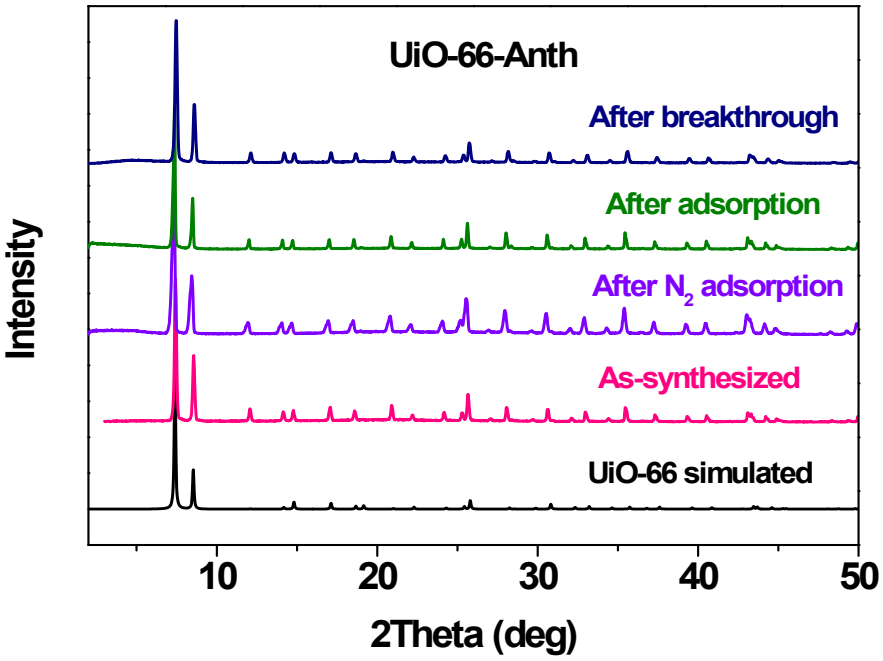

Figure S4. The simulated and experimental PXRD patterns of UiO-66-Anth.

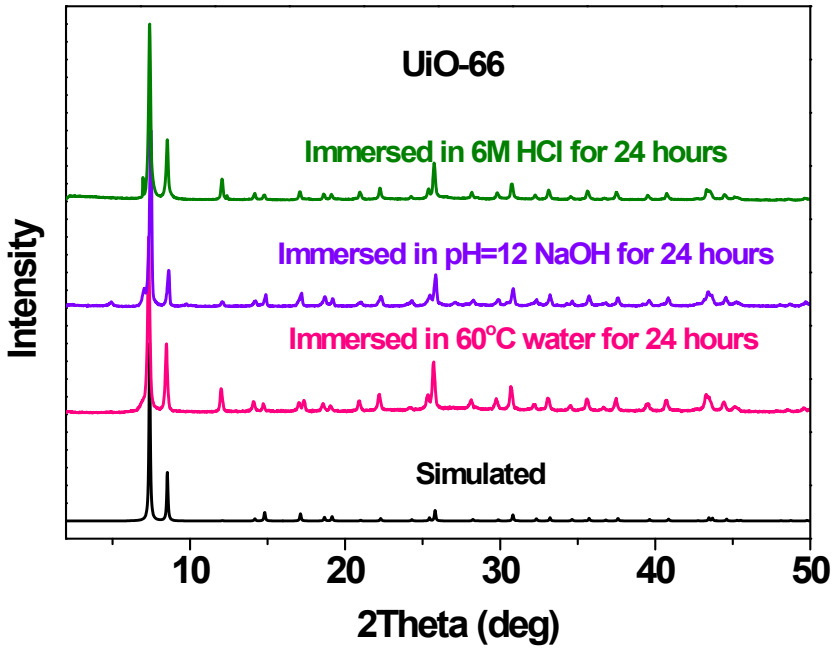

Figure S5. PXRD patterns of UiO-66 immersed in 6M HCl, pH = 12 NaOH and 60 °C H_2O for 24 h, respectively.

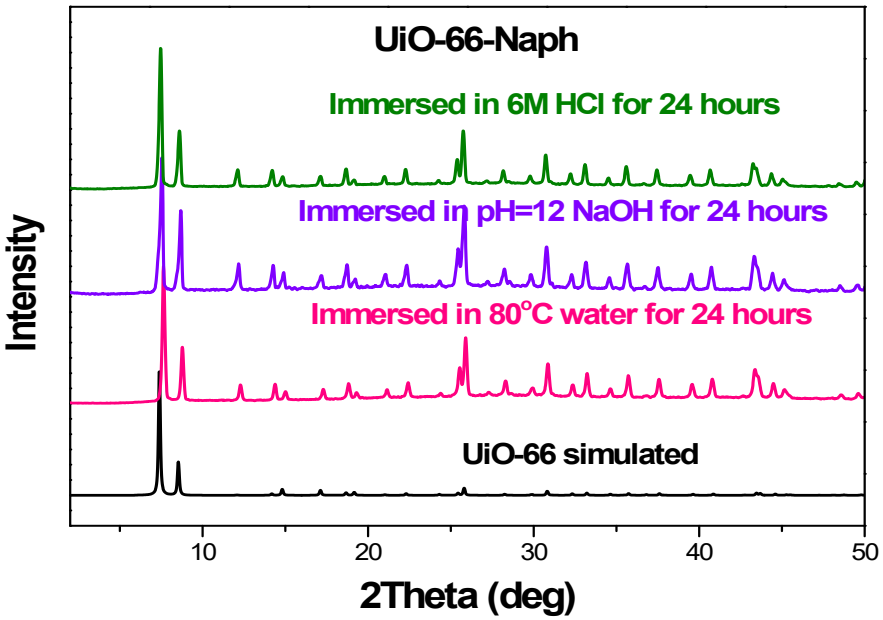

Figure S6. PXRD patterns of UiO-66-Naph immersed in 6M HCl, pH = 12 NaOH and 80 °C water for 24 h, respectively.

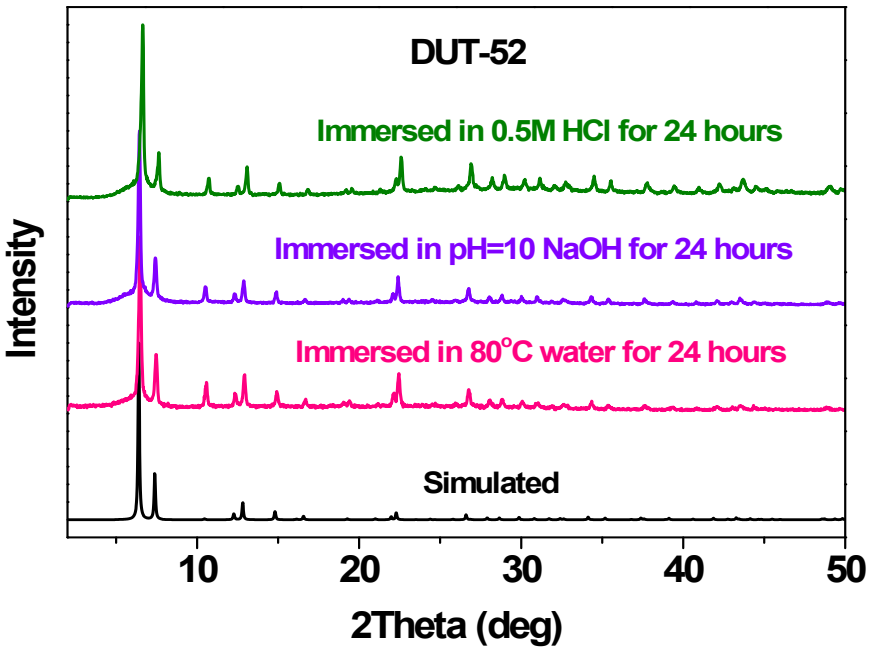

Figure S7. PXRD patterns of DUT-52 immersed in 0.5 M HCl, pH = 10 NaOH and 80 °C water for 24 h, respectively.

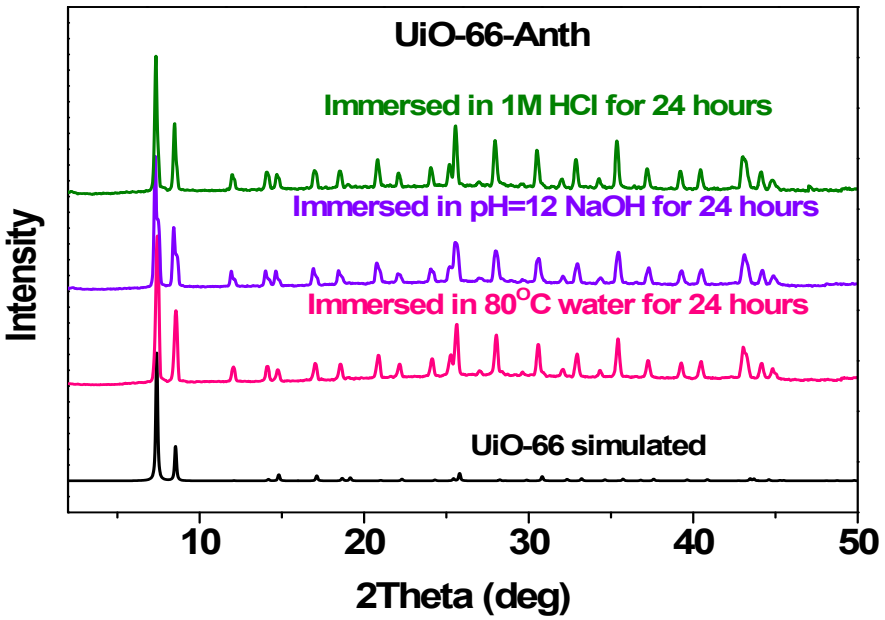

Figure S8. PXRD patterns of UiO-66-Anth immersed in 1M HCl, pH = 12 NaOH and 80 °C water for 24 h, respectively.

S3. Thermal Stability Analysis

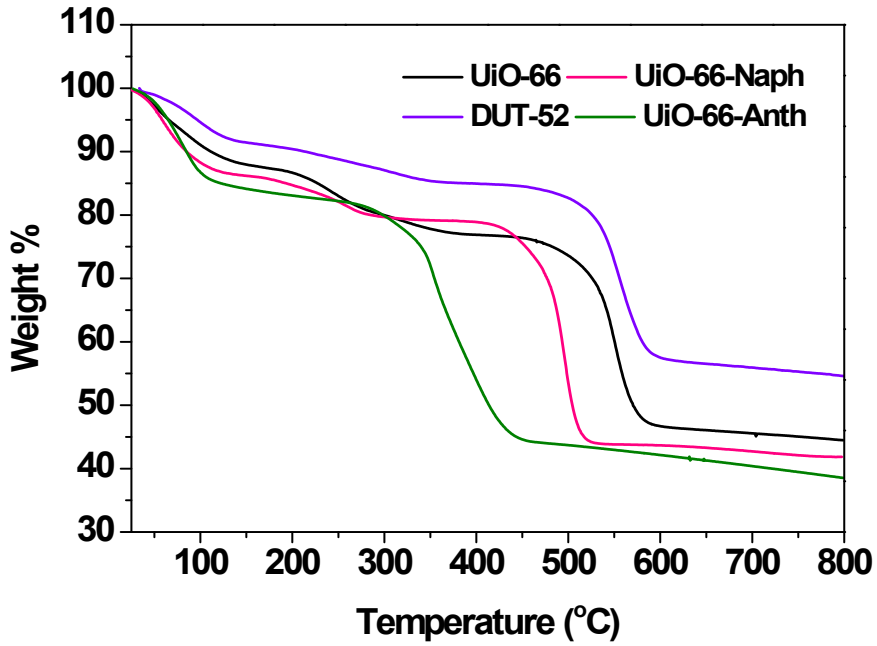

Figure S9. The thermogravimetric analyses of as-synthesized MOFs.

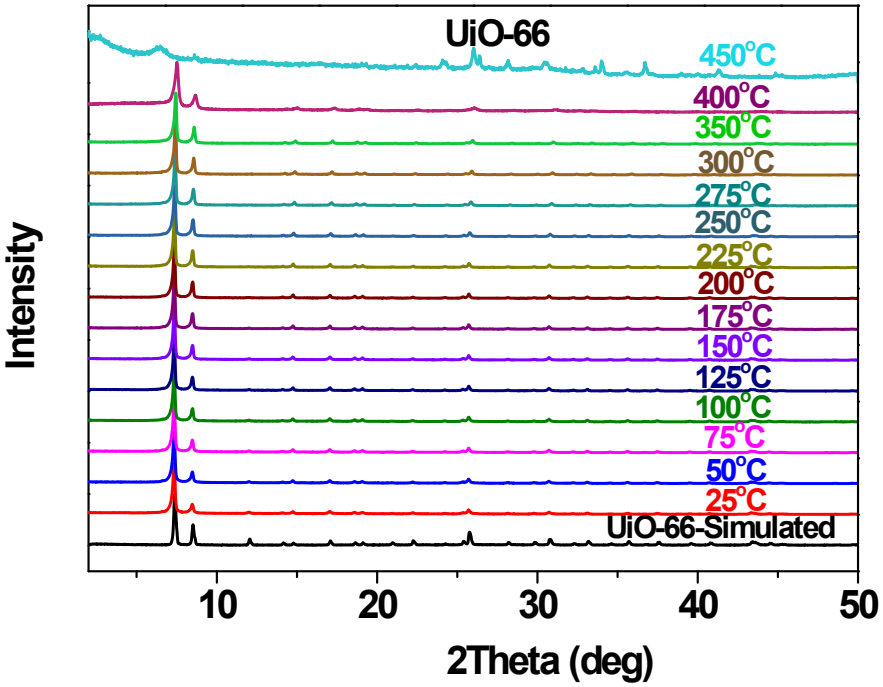

Figure S10. The variable-temperature PXRD patterns of UiO-66.

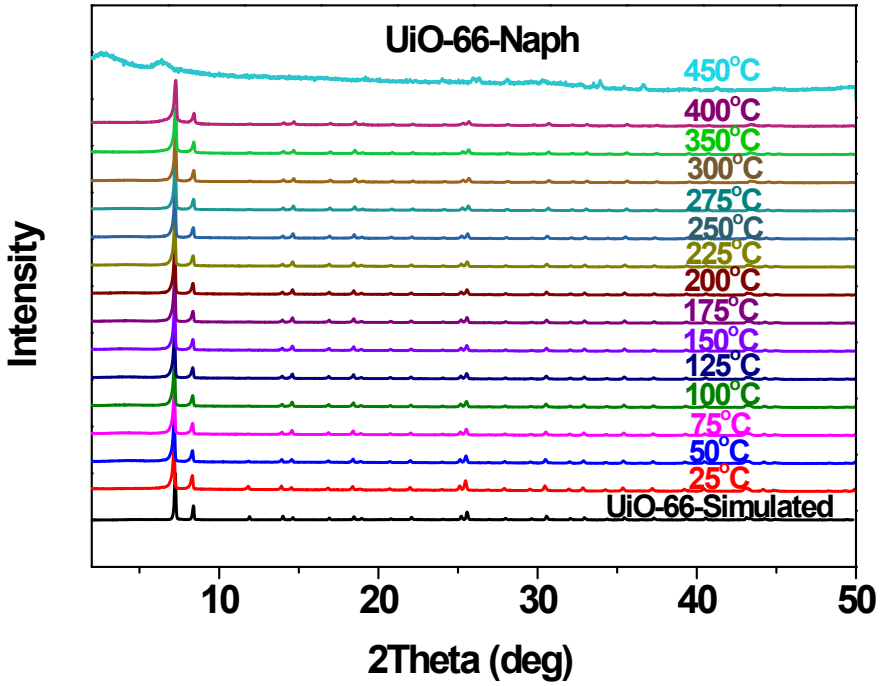

Figure S11. The variable-temperature PXRD patterns of UiO-66-Naph.

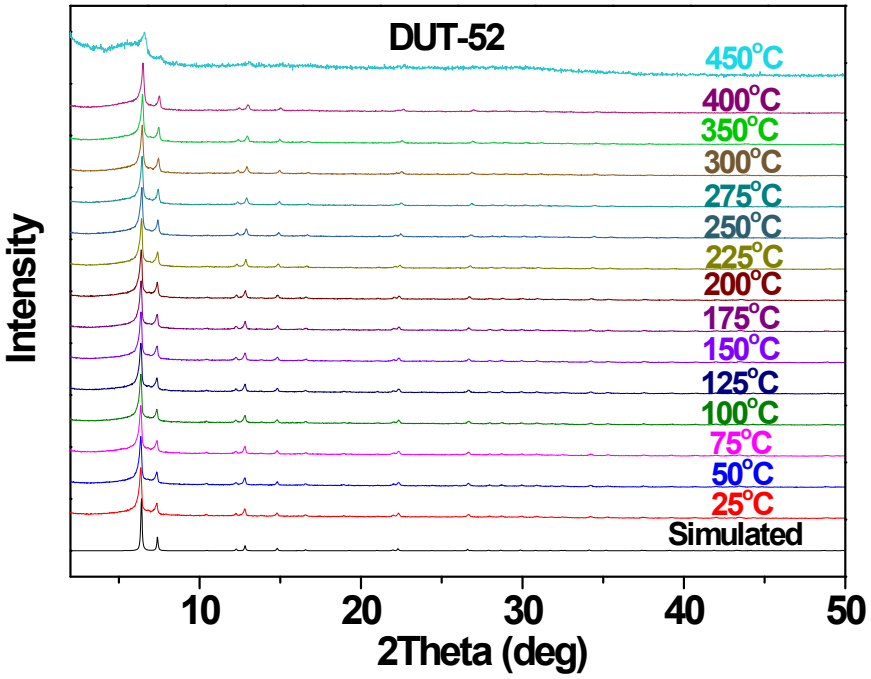

Figure S12. The variable-temperature PXRD patterns of DUT-52.

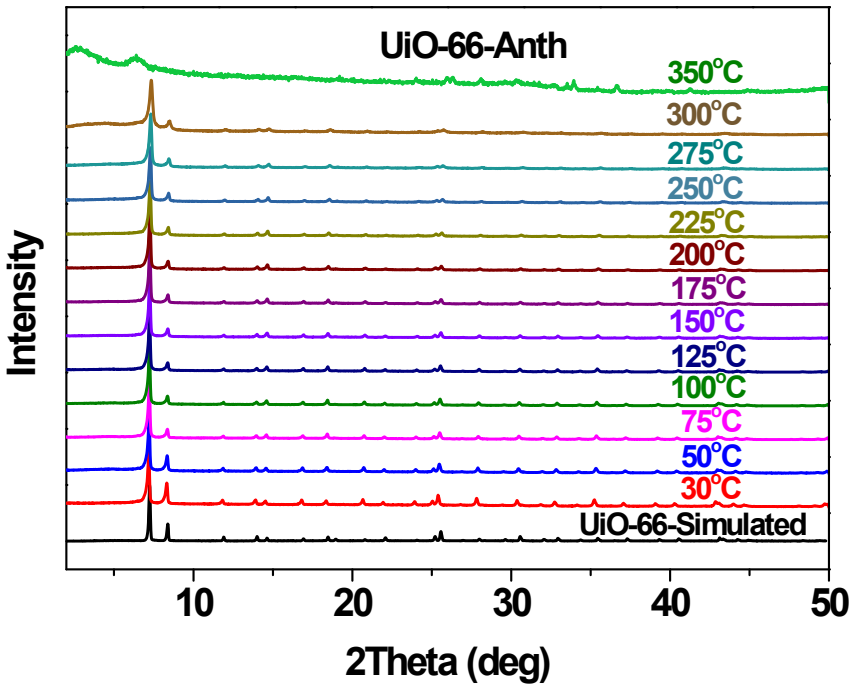

Figure S13. The variable-temperature PXRD patterns of UiO-66-Anth.

S4. Porosity Characterization

N_2 Sorption Isotherm at 77 K: Before gas sorption experiments, the four as-synthesized MOFs and the sample after chemical stability test were immersed in anhydrous acetone for 3 days, during which the solvent was decanted and freshly replenished 3 times a day. The solvent-exchanged samples of the MOFs were activated under vacuum at 100°C for 12 hours. N_2 adsorption isotherms for pressures in the range of 0-1.0 bar were collected by a volumetric method using a quantachrome autosorb IQ3 gas adsorption analyzer. The pore size distribution of UiO-66-Anth is put in Figure S14. The N_2 adsorption isotherms of the MOFs after chemical stability test are showed in Figure S15-Figure S18. BET surface area ($m^2\ g^{-1}$) of four MOFs after treatment are present in **Table S1**. The BET calculation fittings are plotted in Figure S19-Figure S22. The porosity parameters of MOFs are summarized in **Table S4**. The model settings for calculating pore distributions of the MOFs are as follows: 1) UiO-66: N_2 at 77 K on carbon (slit/cylinder/sphere. pores, QSDFT adsorption branch); 2) UiO-66-Naph: N_2 at 77 K on carbon (slit/cylinder/sphere. pores, QSDFT adsorption branch); 3) DUT-52: N_2 at 77 K on carbon (slit/cylinder/sphere. pores, QSDFT adsorption branch); 4) UiO-66-Anth: N_2 at 77 K on carbon (slit/cylinder/sphere. pores, QSDFT adsorption branch).

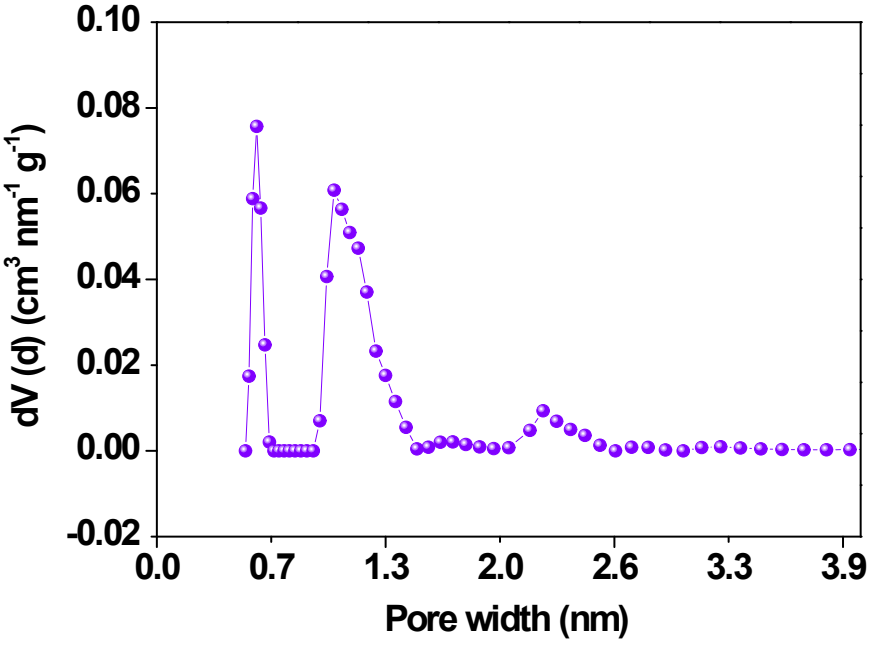

Figure S14. Pore size distribution of UiO-66-Anth calculated from QSDFT mode.

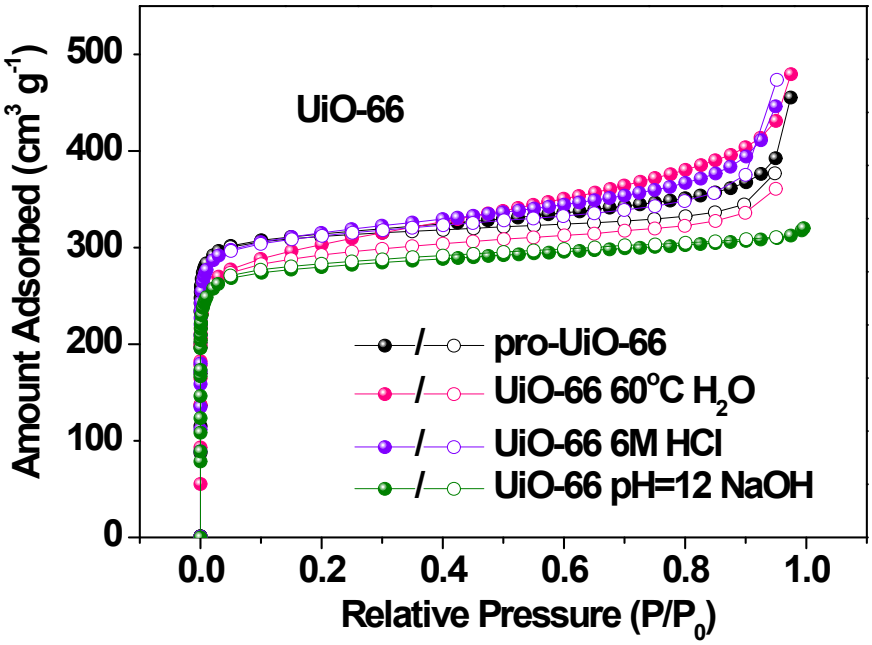

Figure S15. N_2 adsorption isotherms of UiO-66 immersed in 6M HCl, pH = 12 NaOH and 60 °C water for 24 h at 77 K. (Filled symbols, adsorption; empty symbols, desorption.)

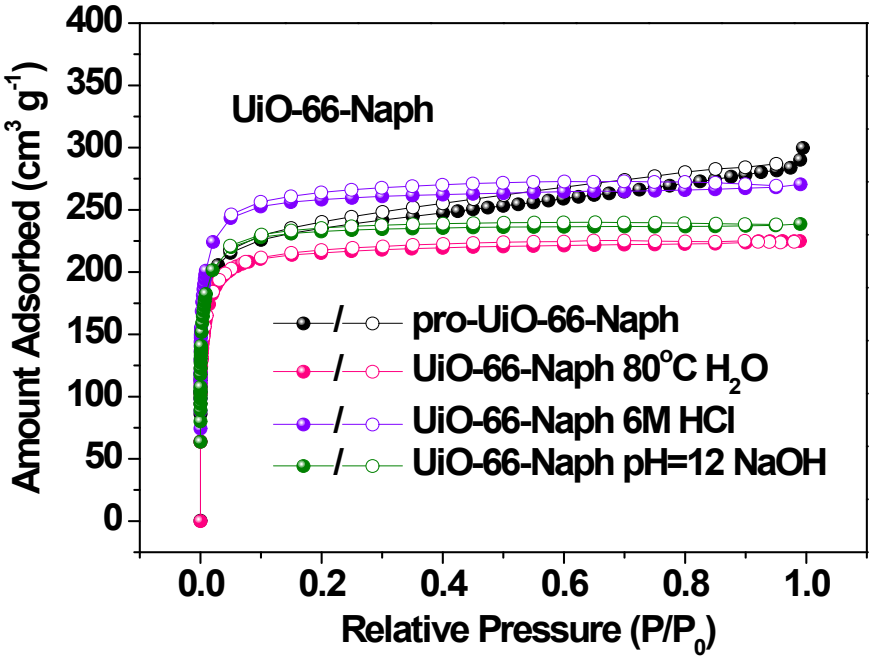

Figure S16. N_2 adsorption isotherms of UiO-66-Naph immersed in 6M HCl, pH = 12 NaOH and 80 °C water for 24 h at 77 K. (Filled symbols, adsorption; empty symbols, desorption.)

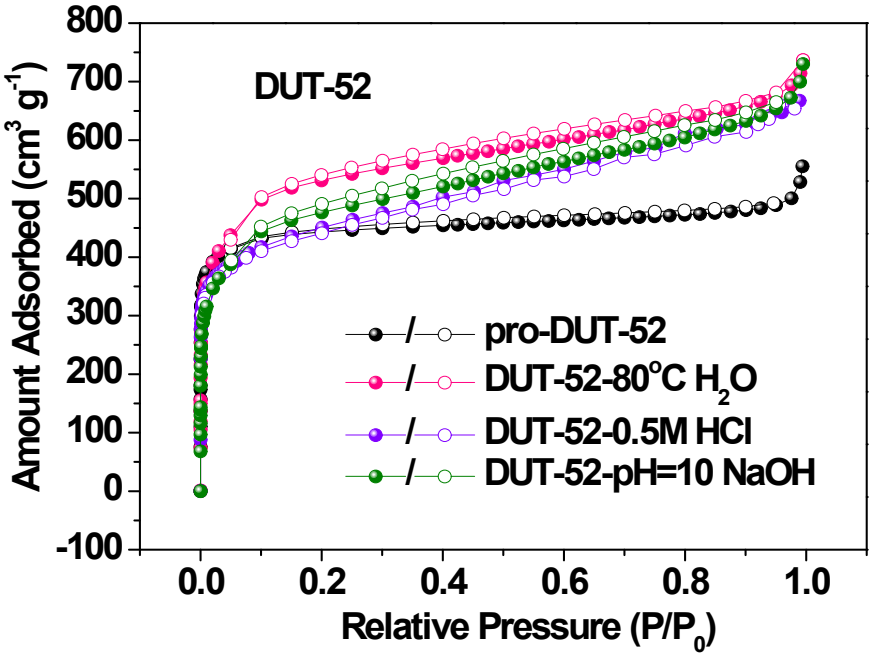

Figure S17. N_2 adsorption isotherms of DUT-52 immersed in 0.5 M HCl, pH = 10 NaOH and 80 °C water for 24 h at 77 K. (Filled symbols, adsorption; empty symbols, desorption.)

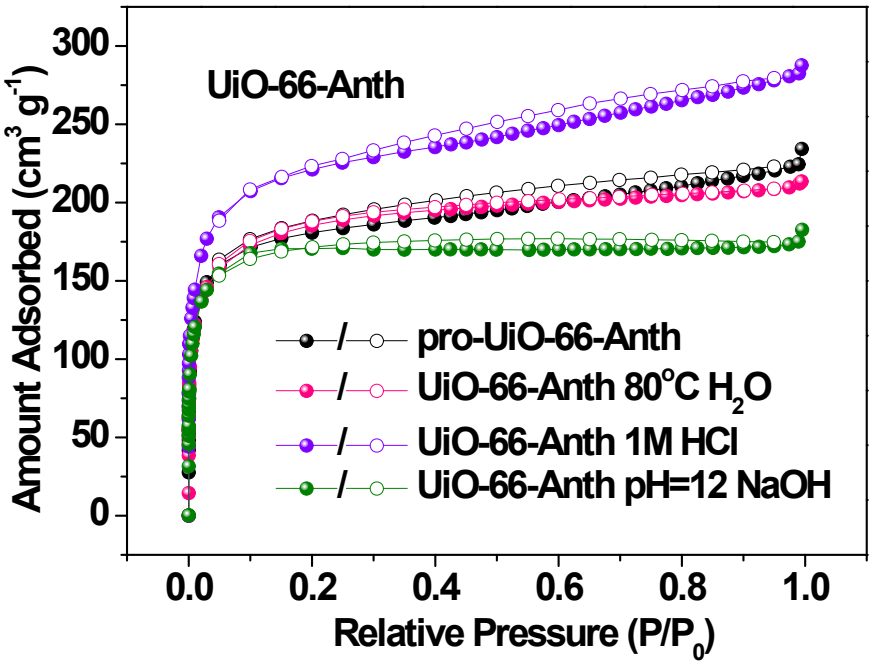

Figure S18. N_2 adsorption isotherms of UiO-66-Naph immersed in 1M HCl, pH = 12 NaOH and 80 °C water for 24 h at 77 K. (Filled symbols, adsorption; empty symbols, desorption.)

Table S1. BET surface area (m^2 g^{-1}) of four MOFs after treatment.

MOF / Treatment	UiO-66	UiO-66-Naph	DUT-52	UiO-66-Anth
Origin	1305	881	1671	676
80 °C H_2O	1232[a]	883	1613	695
HCl	1239[b]	908[b]	1635[c]	641[d]
pH = 12 NaOH	1117	834	1579[e]	664

[a]60 °C. [b]6 M HCl. [c]0.5 M HCl. [d]1 M HCl. [e]pH = 10 NaOH.

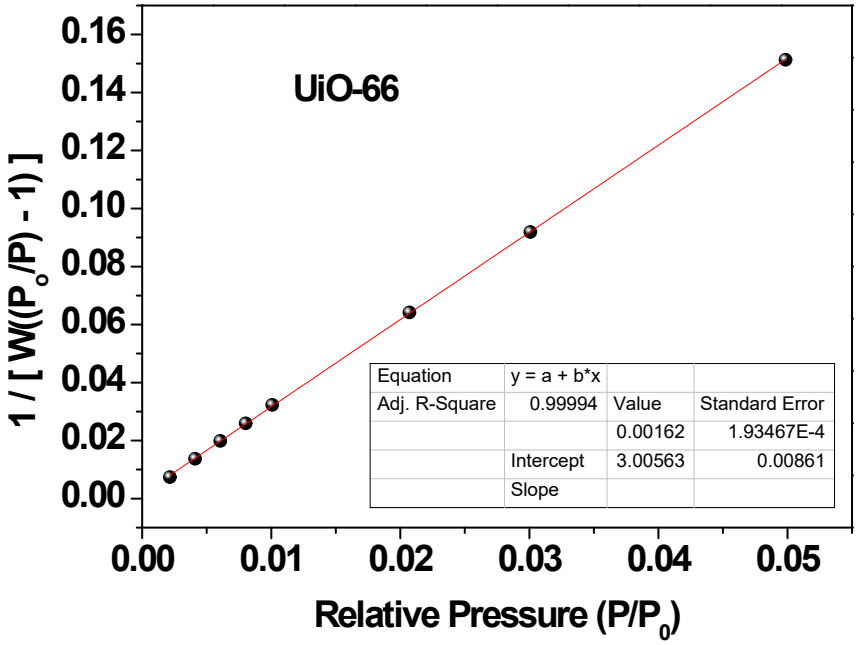

Figure S19. Plot of the linear region on the N_2 isotherm of UiO-66 for the BET equation.

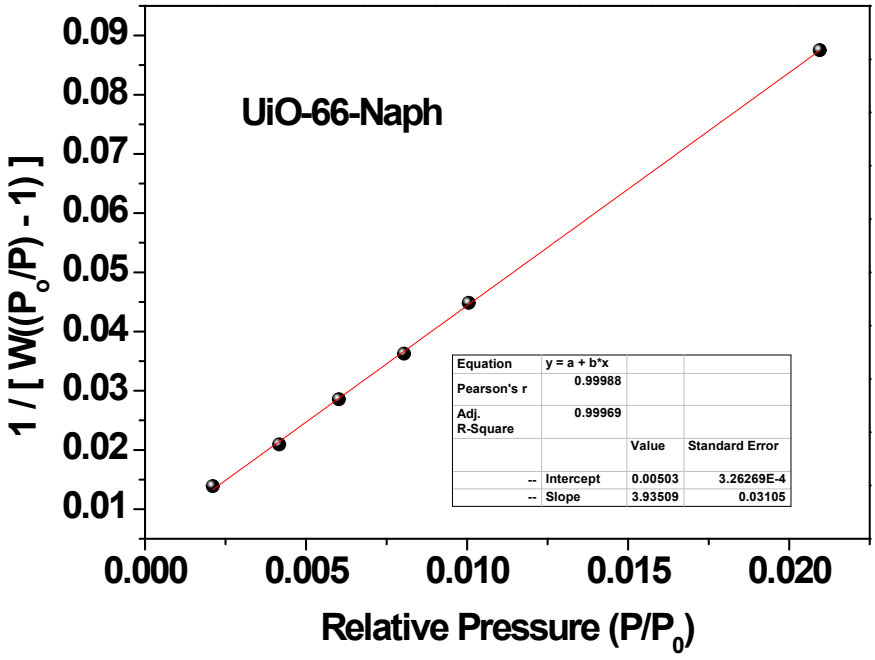

Figure S20. Plot of the linear region on the N_2 isotherm of UiO-66-Naph for the BET equation.

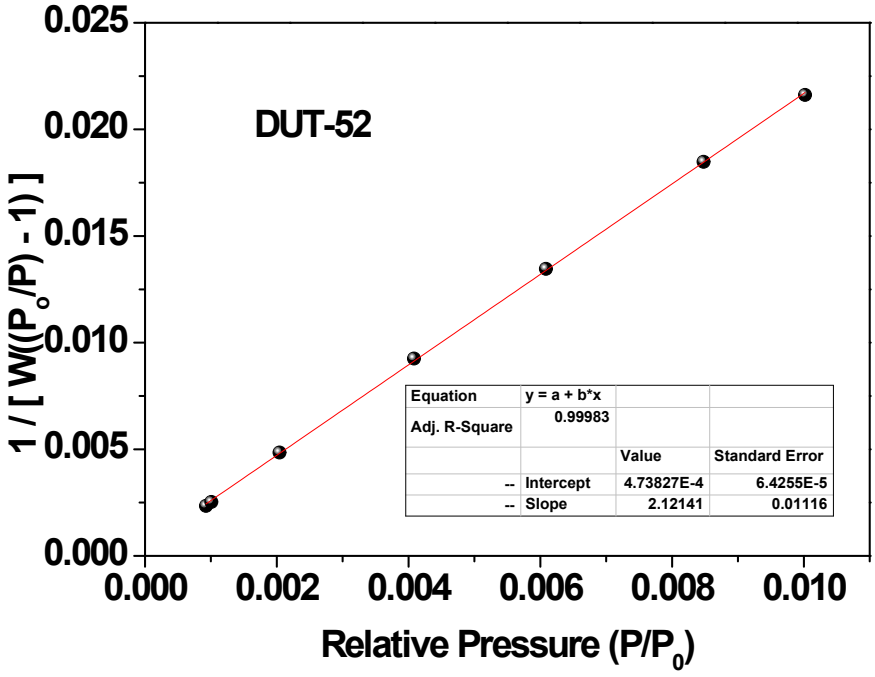

Figure S21. Plot of the linear region on the N_2 isotherm of DUT-52 for the BET equation.

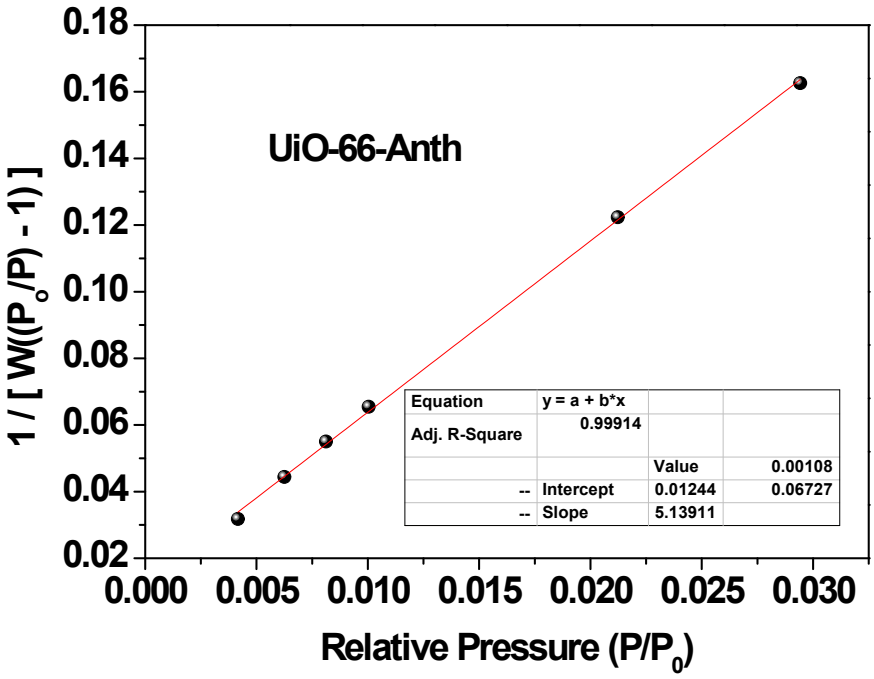

Figure S22. Plot of the linear region on the N_2 isotherm of UiO-66-Anth for the BET equation.

S5. Calculations of Adsorption Isosteric Heat

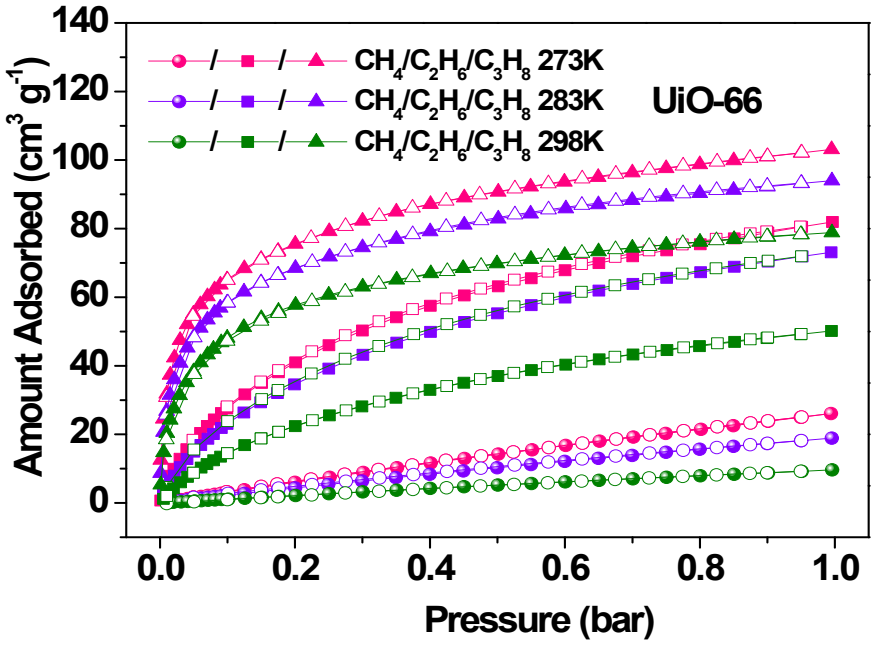

Figure S23. CH_4, C_2H_6 and C_3H_8 adsorption isotherms of UiO-66 at 273, 283 and 298K. (Filled symbols, adsorption; empty symbols, desorption.)

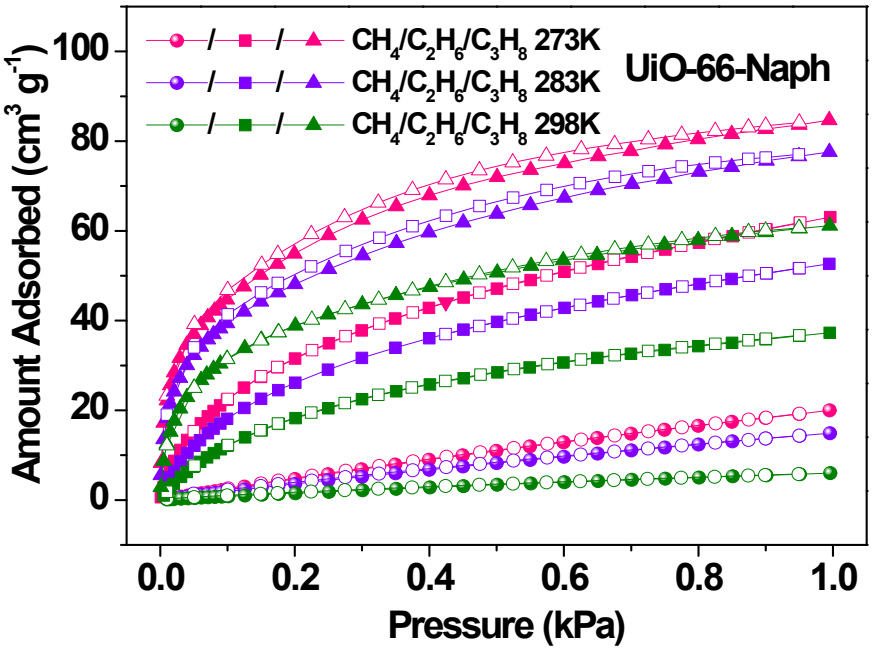

Figure S24. CH_4, C_2H_6 and C_3H_8 adsorption isotherms of UiO-66-Naph at 273, 283 and 298K. (Filled symbols, adsorption; empty symbols, desorption.)

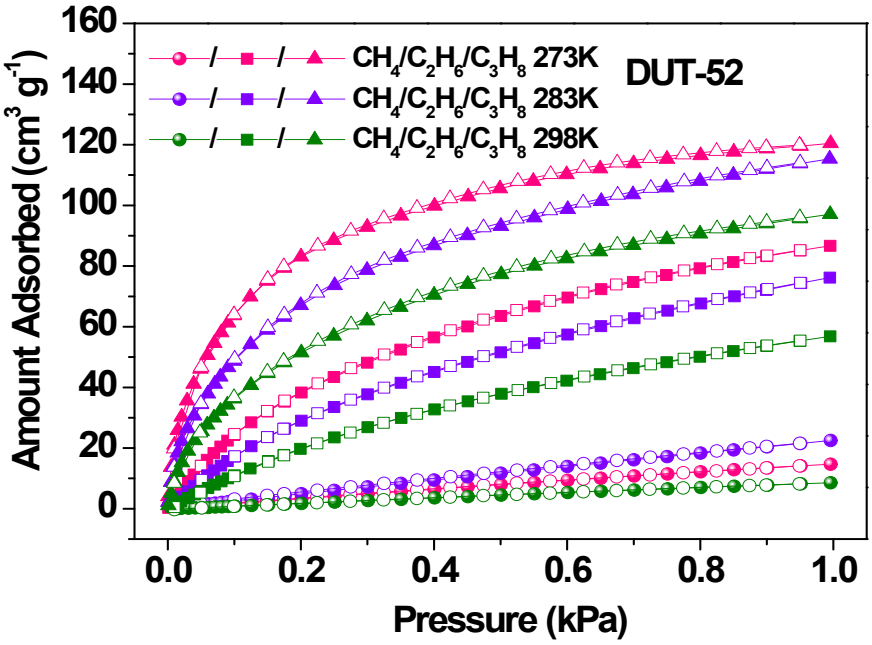

Figure S25. CH_4, C_2H_6 and C_3H_8 adsorption isotherms of DUT-52 at 273, 283 and 298K. (Filled symbols, adsorption; empty symbols, desorption.)

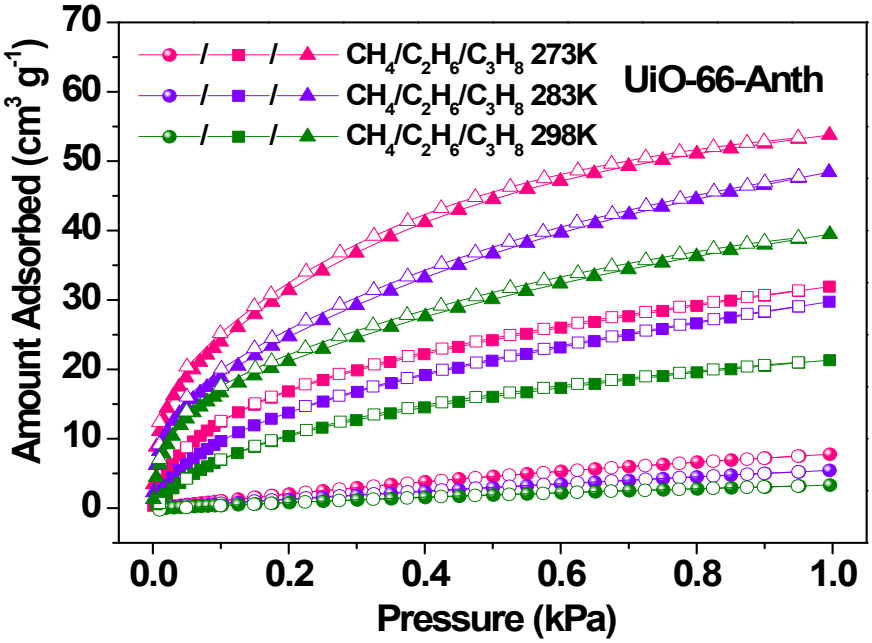

Figure S26. CH_4, C_2H_6 and C_3H_8 adsorption isotherms of UiO-66-Anth at 273, 283 and 298K. (Filled symbols, adsorption; empty symbols, desorption.)

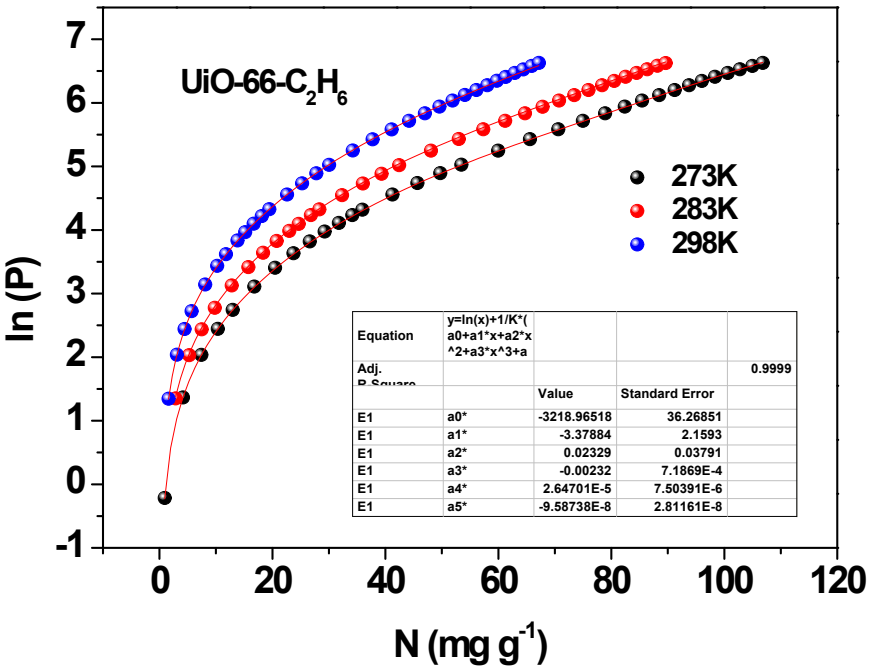

Equation	y=ln(x)+1/K*(a0+a1*x+a2*x^2+a3*x^3+a			
Adj. R Square				0.9999
		Value	Standard Error	
E1	a0*	-3218.96518	36.26851	
E1	a1*	-3.37884	2.1593	
E1	a2*	0.02329	0.03791	
E1	a3*	-0.00232	7.1869E-4	
E1	a4*	2.64701E-5	7.50391E-6	
E1	a5*	-9.58738E-8	2.81161E-8	

Figure S27. C_2H_6 virial fitting (lines) of the adsorption isotherms (points) of UiO-66 measured at 273, 283 and 298 K.

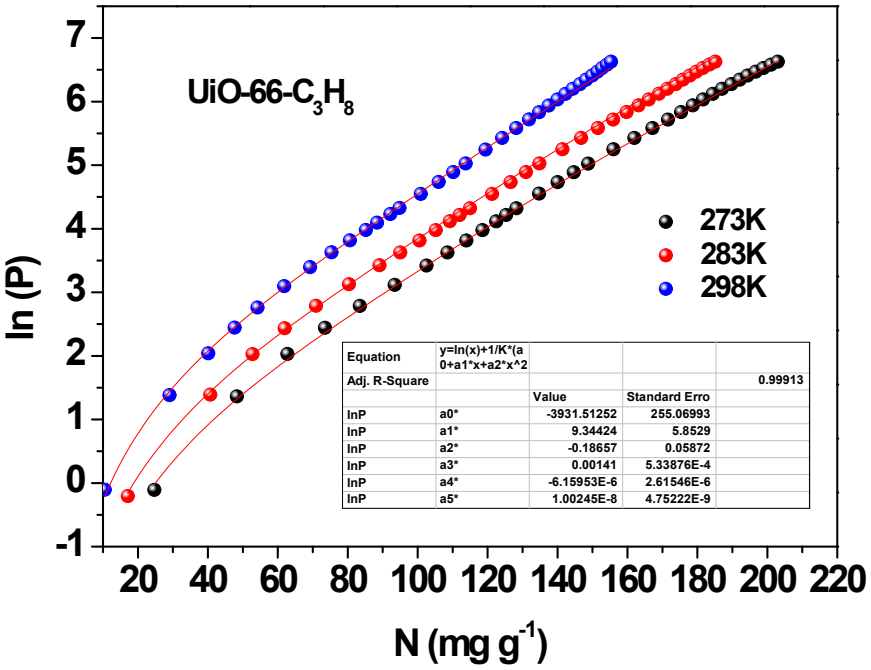

Figure S28. C_3H_8 virial fitting (lines) of the adsorption isotherms (points) of UiO-66 measured at 273, 283 and 298 K.

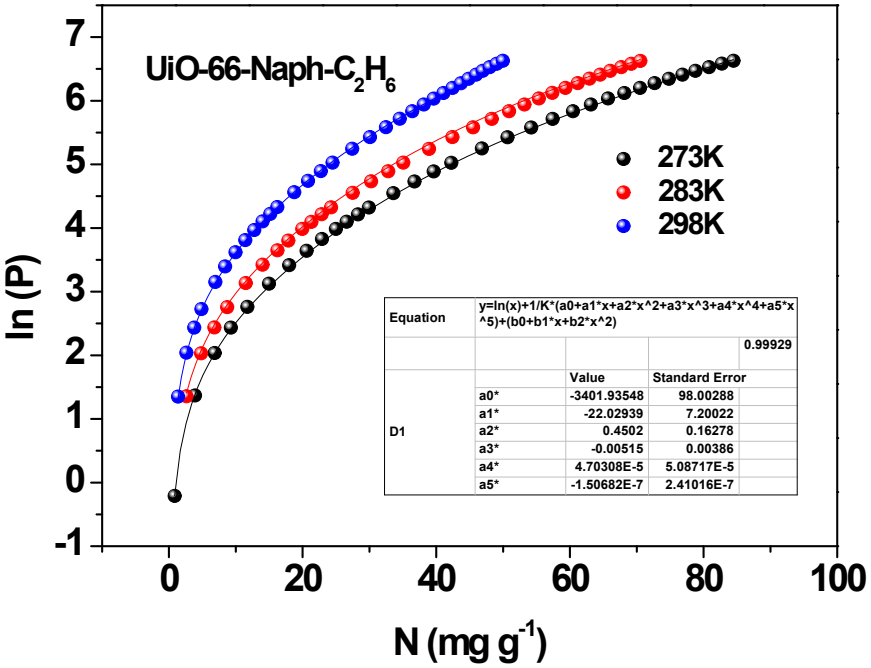

Figure S29. C_2H_6 virial fitting (lines) of the adsorption isotherms (points) of UiO-66-Naph measured at 273,283 and 298 K.

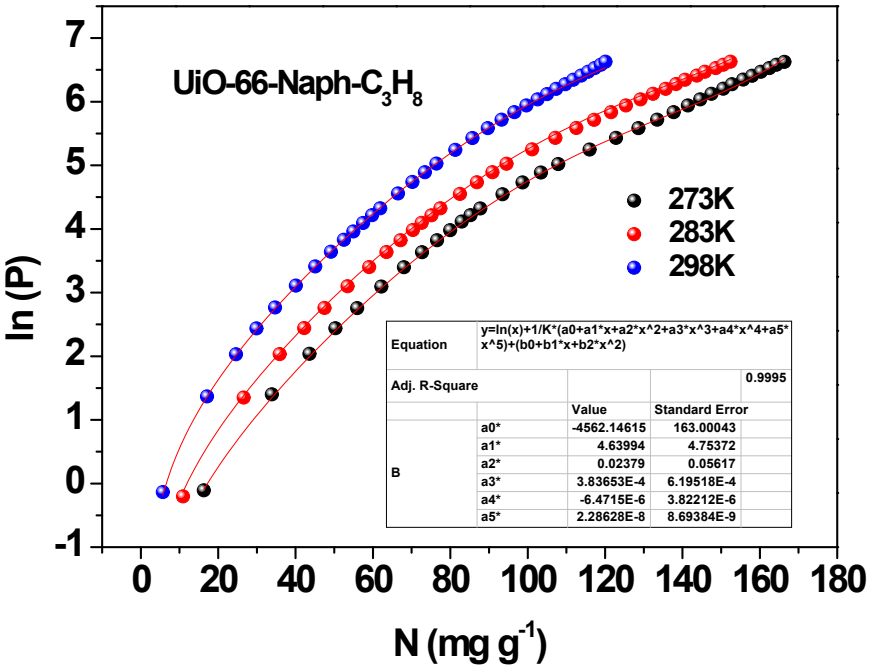

Figure S30. C_3H_8 virial fitting (lines) of the adsorption isotherms (points) of UiO-66-Naph measured at 273, 283 and 298 K.

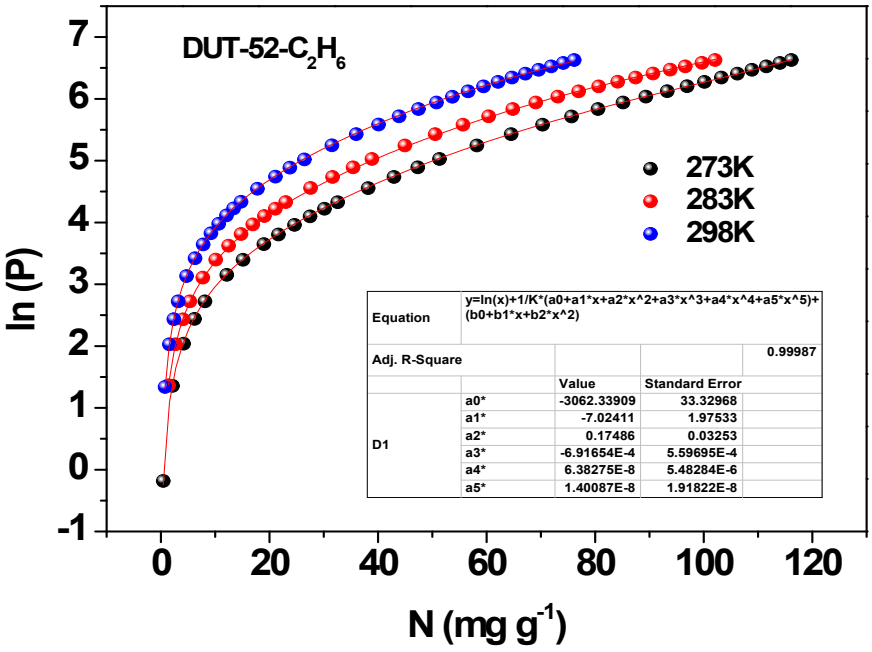

Figure S31. C_2H_6 virial fitting (lines) of the adsorption isotherms (points) of DUT-52 measured at 273, 283 and 298 K.

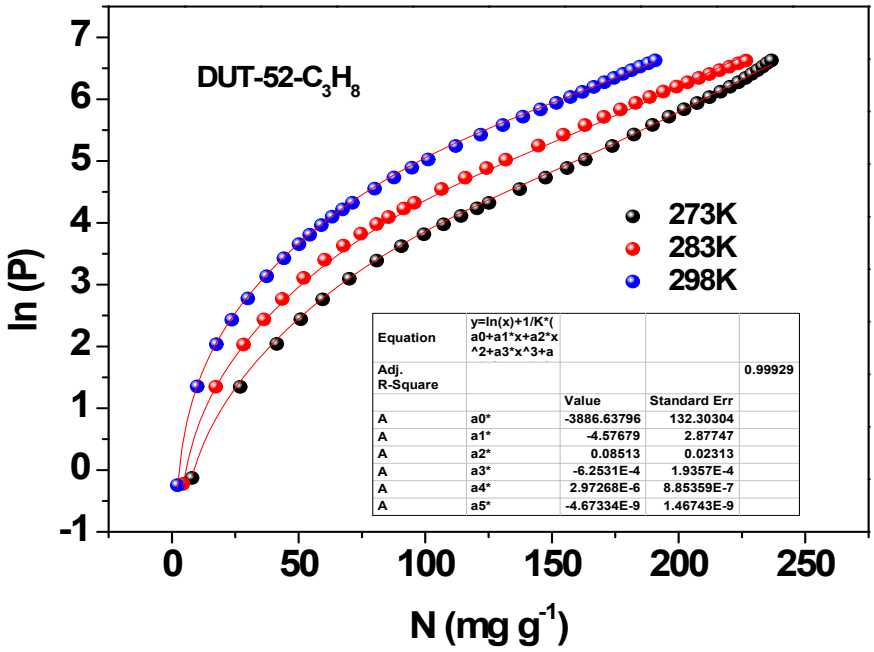

Figure S32. C_3H_8 virial fitting (lines) of the adsorption isotherms (points) of DUT-52 measured at 273, 283 and 298 K.

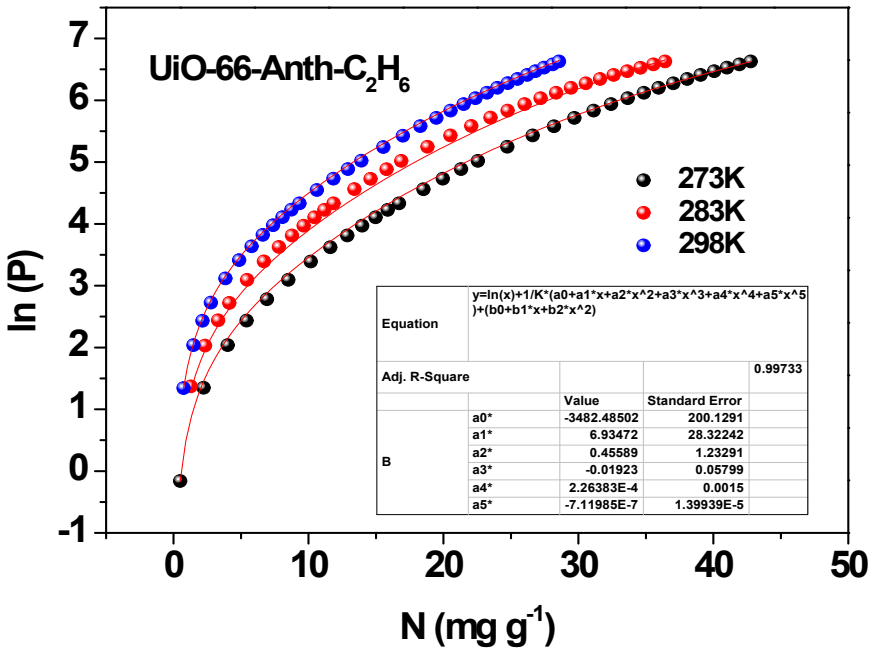

Figure S33. C_2H_6 virial fitting (lines) of the adsorption isotherms (points) of UiO-66-Anth measured at 273, 283 and 298 K.

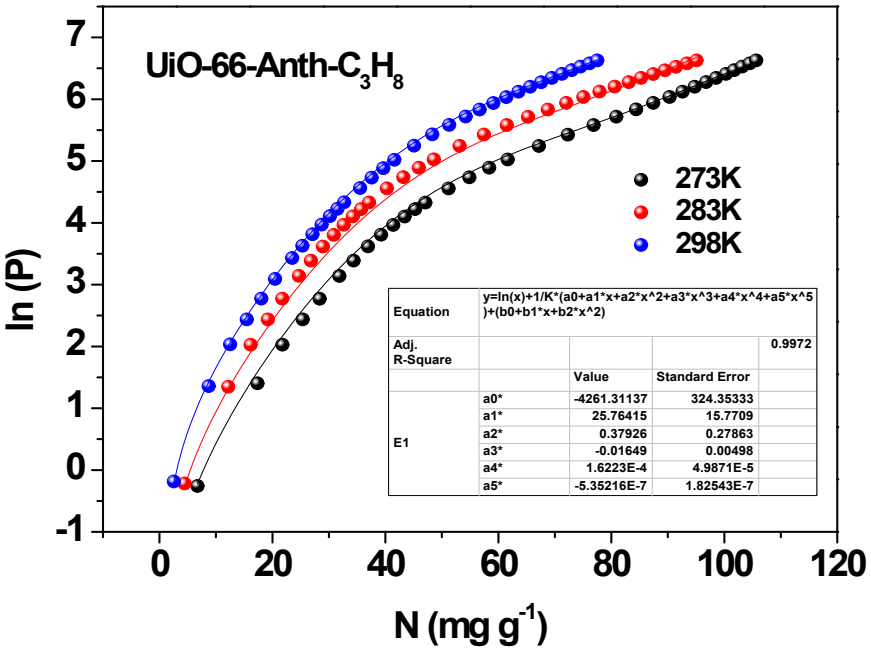

Figure S34. C_3H_8 virial fitting (lines) of the adsorption isotherms (points) of UiO-66-Anth measured at 273, 283 and 298 K.

S6. Comparison of C_3/C_1 IAST Selectivity Enhancing Effects

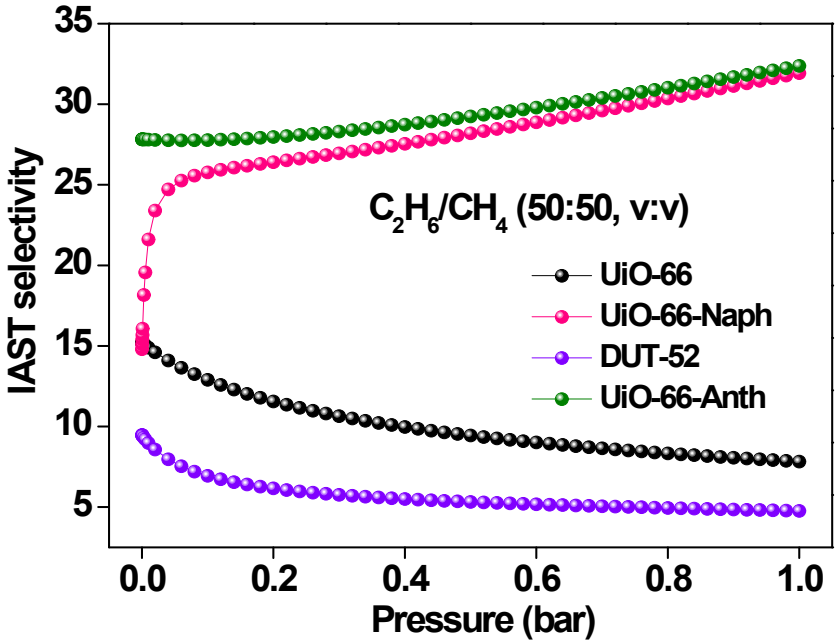

Figure S35. IAST selectivity of the MOFs for C_2H_6/CH_4 (50:50, v:v).

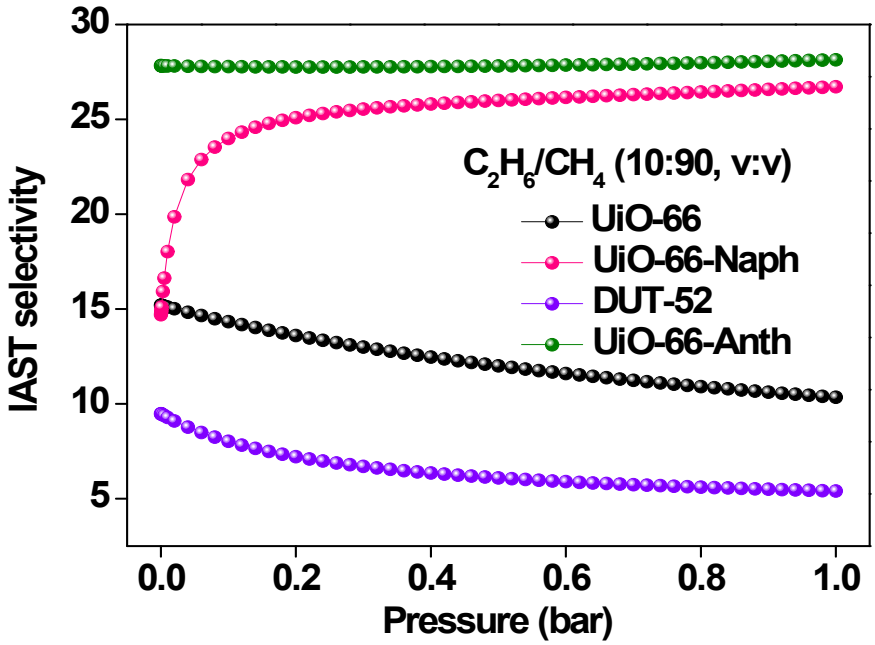

Figure S36. IAST selectivity of the MOFs for C_2H_6/CH_4 (10:90, v:v).

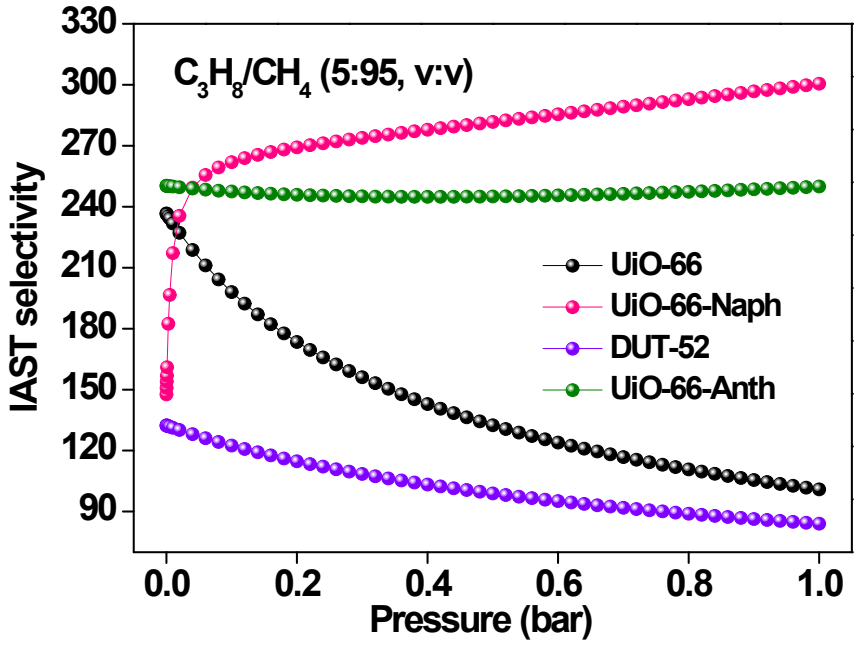

Figure S37. IAST selectivity of the MOFs for C_3H_8/CH_4 (5:95, v:v).

C_3/C_1 IAST selectivity increase are evaluated by the increase ratio, which is calculated by the following equation.

$$C_3/C_1\ IAST\ selectivity\ increase\ ratio = \frac{improved\ IAST\ selectivity\ -\ original\ IAST\ selectivity}{original\ IAST\ selectivity} \times 100\%$$

Table S2. Comparison of C_3/C_1 IAST selectivity increase effects in porous materials.

C_3/C_1 IAST Selectivity Enhancing Effect	MOFs	C_3/C_1 IAST selectivity (50:50)	C_3/C_1 IAST selectivity increase ratio (50:50)	Reference
Aromatic effect	UiO-66	65	0	This work
	UiO-66-Naph	741	1040%	
	DUT-52	48	-26%	
	UiO-66-Anth	535	723%	
Macrocyclic effect	P5-CMP-1	180[a]	0	1
	P5-CMP-2	189[a]	5%	
Configurations effect (①/②,③/④); Pore size effect (①/③, ②/④)	①sPI−A−H	66.4		2
	②sPI−M−H	82.0		
	③sPI−A−B	204.7		
	④sPI−M−B	217.4		
Functional group effect	MPI	284	205%	3
	MPI-S	93	0	
	MPI-Ag	94	1%	
Fluorine-functionalization effect	PAN-5H	176.2	0	4
	PAN-5F	372.3	111%	
	PAN-2F	260.5	48%	
	PAN-2$(CF)_3$	198.1	12%	
Monomers size effect	PAN-T1	190.8[a]	37%	5
	PAN-T2	139.0[a]	0	
Donor position effect	eea-MOFs	136[b]	0	6
	rtl-MOFs	156[b]	15%	
Coordination modes effect	JLU-Liu5	107.8[b]	0	7
	JLU-Liu6	274.6[b]	155%	
Temperature effect (400,500,600 °C)	ZnP-CTF-400	290	0	8
	ZnP-CTF-500	513	77%	
	ZnP-CTF-600	733	153%	
Temperature effect (500,550,600 °C)	CTF-BIB-1	386.6	127%	9
	CTF-BIB-2	311.2	82%	
	CTF-BIB-3	170.5	0	
Temperature effect (600,700,800 °C)	NAC 600	406.0	99%	10
	NAC 700	501.9	147%	
	NAC 800	203.6	0	

Regulator effect	Zn2(TCPP)(DPB) (1) Zn2(TCPP)(DPB) (2)	122.3 41.4	195% 0	11
Metal ion effect	LIFM-13(Mg) LIFM-13(Co) LIFM-13(Ni) LIFM-13(Zn)	528.9 161.5 252.2 127.8	314% 26% 97% 0	12
Metalloporphyrin effect (110kPa)	PAF-40 PAF-40-Fe PAF-40-Mn	48.2 56 246	0 16% 410%	13

[a]The C_3/C_1 ratio is 10:90. [b]The C_3/C_1 ratio is 5:95.

Table S3. $CH_4/C_2H_6/C_3H_8$ adsorption and separation performance for some benchmark adsorbents at 298 K and 100 kPa.

MOFs	CH_4 ($mmol^{-1}$)	C_2H_6 ($mmol^{-1}$)	C_3H_8 ($mmol^{-1}$)	C_3/C_1 IAST selectivity (298K, 50:50)	C_2/C_1 IAST selectivity (298K, 50:50)	Reference
UiO-66	0.60	1.67	1.79	65	8	This
UiO-66-Naph	0.38	1.24	1.39	741	32	work
DUT-52	0.54	1.89	2.21	48	5	
UiO-66-Anth	0.21	0.70	0.90	535	32	
ANPC-1-800	1.45	6,84	9.74	110.4	14.5	14
ANPC-2-700	1.12	4.88	8.80	162.5	13.5	
ANPC-2-800	1.15	4.94	11.5	120.2	11.9	
BSF-1	0.66	1.17	0.99	353	23	15
FJI-C4	1.15	2.21	1.63	293.4	39.7	16
FJI-H22	0.88	1.49	1.10	145.23	11.95	17
JLU-Liu5	1.00	2.37	1.59	107.8	17.6	7
JLU-Liu6	0.81	1.63	1.30	274.6	20.4	
JLU-Liu7	1.06	3.57	2.57	128.5	50.4	18
JLU-Liu38	0.48	4.96	8.39	98	12.5	19
JUC-100	0.64	3.07	3.09	80	11	20
JUC-103	0.73	2.85	2.77	55	8	
JUC-106	0.51	2.61	2.59	75	13	
UTSA-35a (296K)	0.43	2.43	2.97	80	20	21
MFM-202a	0.45	4.21	6.76	87	10	22
InOF-1	0.64	4.14	4.25	90	17	23
RT-MIL-100(Fe)	0.36	2.22	6.78	33.3(5:85)	6(10:85)	24
MIL-101-Cr	0.49	1.59	3.35	84.3	22.5	25
MIL-101-Fe	0.45	1.25	3.29	24.9	15.4	
MIL-101-Fe-NH_2	0.46	1.35	3.32	42.5(5:85)	11.6(10:85)	
A-AC-3	1.38	7.09	11.34	76.6(1:4)	16.9(1:4)	26
A-AC-4	1.18	6.59	11.76	88.8(1:4)	15.1(1:4)	
A-AC-5	0.98	5.00	9.12	9.31(Uptake ratio)	5.10(Uptake ratio)	
sPI-A-H	0.39	1.59	2.00	66.7	13.3	2
SBA-15	0.11	0.56	1.24	/	4.9(Uptake ratio,303K)	27

S7. Breakthrough Experiments

Transient breakthrough experiments for the separation of $CH_4/C_2H_6/C_3H_8$ (85:10:5, v:v:v) were carried out in a fixed bed. The column (6 mm inner diameter × 150 mm) was filled with ~1g pre-activated sample for the experiment using a ternary component gases mixture. Before filled in the column, the samples were activated at 373 K for 8 h under vacuum conditions. After filling the column, the column was purged with a He flow for 1 h. The flow rates (5 mL min^{-1} at 298 K and 1 bar) of gases were regulated by mass flow controllers. Then the $CH_4/C_2H_6/C_3H_8$ gas mixture with 5 mL min^{-1} was introduced to the column. The outlet composition was continuously monitored by a gas chromatograph (FULI GC9790 Plus) until a complete breakthrough was achieved. The sample was regenerated with a He flow (5 mL min^{-1}) at 373 K for 2 h before each cyclic experiment.

The capture capacity (also called capture amount) is determined as follows:[28, 29]

$$q_i = \frac{v \times V_i\%}{22.4 \times m} \int_0^t (1 - \frac{C}{C_0}) dt$$

Where q_i is the capture amount of gas i (mmol g^{-1}), v is the flow rate of the gas mixture (mL min^{-1}), $V_i\%$ is molar fraction of gas i, t is the adsorption time (min), C_0 and C are the inlet and outlet gas concentration, respectively, and m is the mass of the adsorbent (g).

The separation potential (Δq) represents the difference of moles of component 1 (the more strongly adsorbed gas) and component 2 (the less strongly adsorbed gas) adsorbed in the per g of adsorbents in the fixed bed. Δq is calculated by following the equation below proposed by Krishna.[30, 31]

$$\Delta q = q_1 - q_2 \frac{y_1}{y_2}$$

Where q_1 and q_2 are the capture amount (units: mmol g^{-1}) for mixture adsorption, calculated from the breakthrough curves, respectively, and y_1 and y_2 are the component content of the gases.

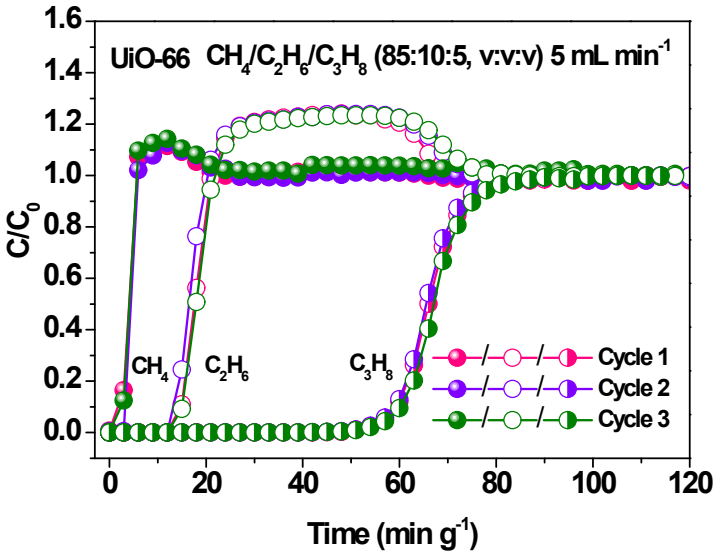

Figure S38. Three cycles of transient breakthrough tests of a $CH_4/C_2H_6/C_3H_8$ (85:10:5, v:v:v) mixture for UiO-66.

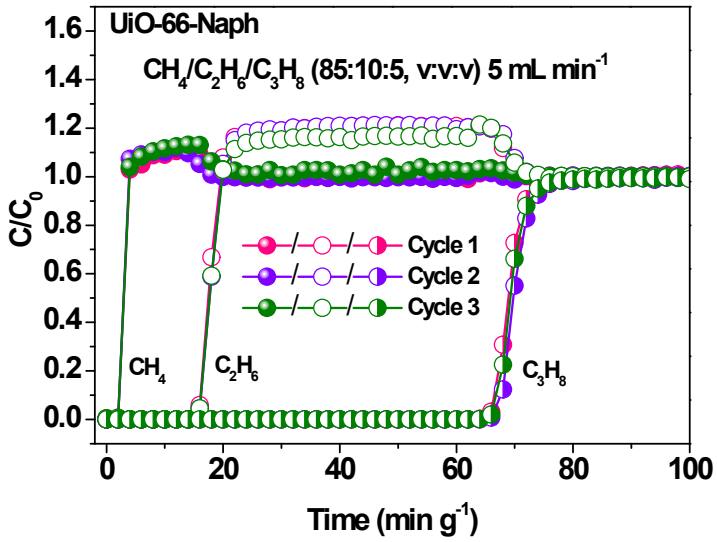

Figure S39. Three cycles of transient breakthrough tests of a $CH_4/C_2H_6/C_3H_8$ (85:10:5, v:v:v) mixture for UiO-66-Naph.

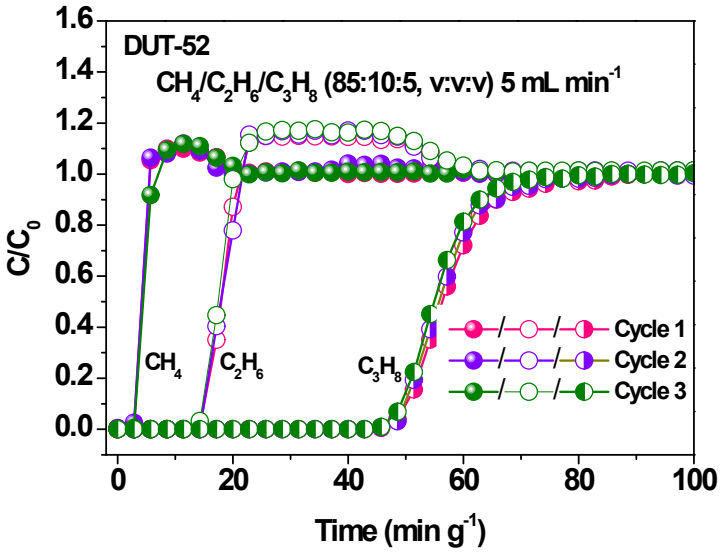

Figure S40. Three cycles of transient breakthrough tests of a $CH_4/C_2H_6/C_3H_8$ (85:10:5, v:v:v) mixture for DUT-52.

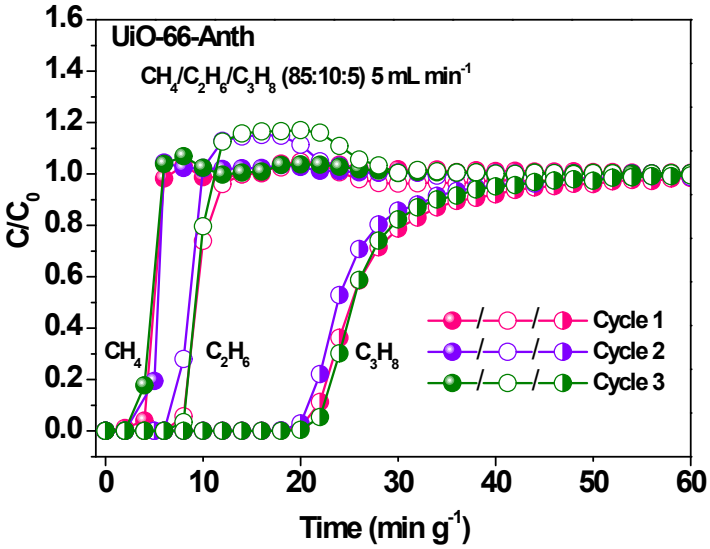

Figure S41. Three cycles of transient breakthrough tests of a $CH_4/C_2H_6/C_3H_8$ (85:10:5, v:v:v) mixture for UiO-66-Anth.

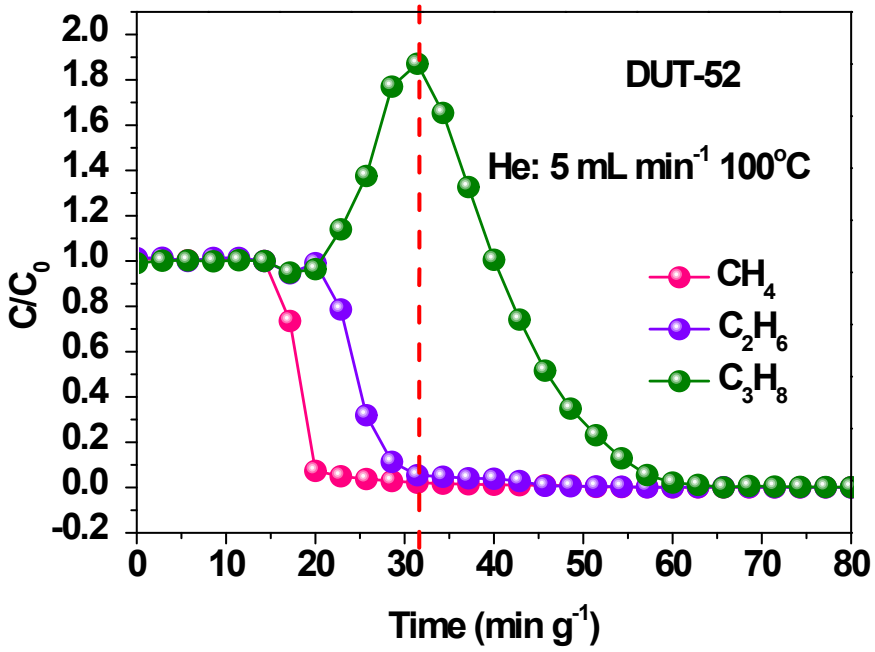

Figure S42. Desorption curves of DUT-52 for the $CH_4/C_2H_6/C_3H_8$ (85:10:5, v:v:v) mixture separation.

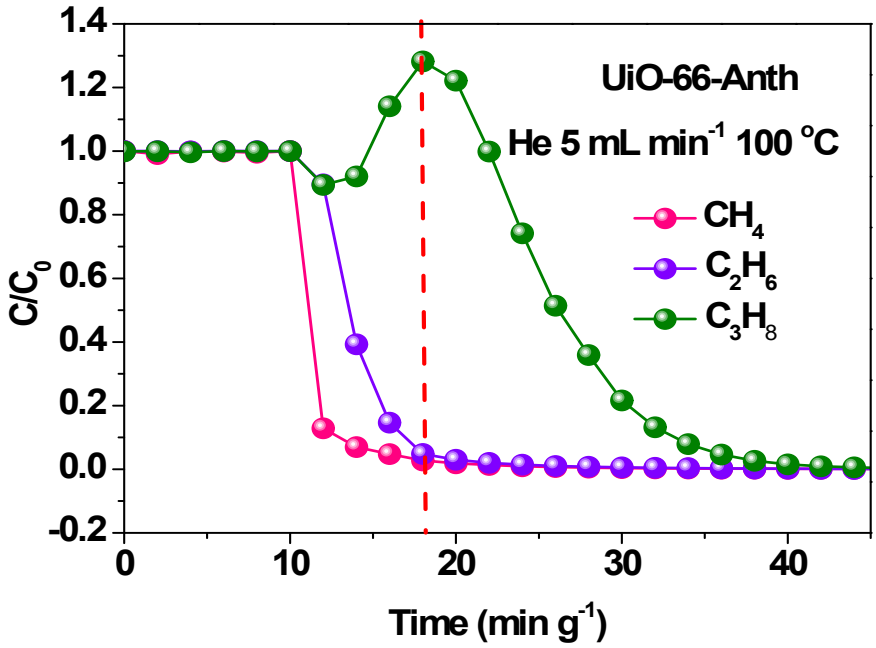

Figure S43. Desorption curves of UiO-66-Anth for the $CH_4/C_2H_6/C_3H_8$ (85:10:5, v:v:v) mixture separation.

Table S4. Summary of MOF BET surface areas, pore volumes, C_2/C_1 & C_3/C_1 IAST selectivities, isosteric heats (Q_{st}), breakthrough productivities (for CH_4), breakthrough capture capacities (for C_2H_6 and C_3H_8) and separation potentials (Δq for C_3H_8/CH_4).

MOF	BET surface area ($m^2\ g^{-1}$)	V_p ($cm^3\ g^{-1}$)	Pore size (nm)	C_2/C_1 IAST selectivity (10: 95 / 50: 50)	C_3/C_1 IAST selectivity (5: 95 / 50: 50)	Q_{st} (kJ mol^{-1})		Breakthrough productivity (mmol g^{-1})	Breakthrough capture capacity (mmol g^{-1})		$\Delta q(C_3H_8/CH_4)$
						C_2H_6	C_3H_8	CH_4	C_2H_6	C_3H_8	
UiO-66	1305	0.47	0.86,1.11	10/ 8	100/ 65	26.76	32.69	1.65	0.18	0.74	0.71
UiO-66-Naph	881	0.40	0.55,1.05	26/ 32	300/ 741	28.29	37.92	2.25	0.18	0.77	0.75
DUT-52	1641	0.70	1.03,1.73	6/ 5	84/ 48	24.57	28.89	2.08	0.28	0.63	0.20
UiO-66-Anth	676	0.32	0.57,1.01	28/ 32	250 /535	28.95	35.16	0.17	0.15	0.29	0.61

S8. Theoretical Calculations

Grand canonical Monte Carlo (GCMC) calculations were performed with the Sorption module of Materials Studio.[32] One unit cell was used. Four H^+ is add to each Zr_6O_8 cluster to balance the charge.[33] The MOF structures are all optimized with the Forcite module using Universal force field (UFF). The charges were determined by the charge equilibration (QEq) approach.[34] The structures and charges of CH_4, C_2H_6, and C_3H_8 were prepared with Dmol^3 module (Figure S45).[35] The Perdew-Burke-Ernzerhof (PBE) functional was used under the generalized gradient approximation (GGA) functional with the double-ξ numerical polarization (DNP) basis set. The tolerances of energy, gradient, and displacement convergence were 1.0×10^{-5} hartree, 2×10^{-3} hartree $Å^{-1}$, and 5×10^{-3} Å, respectively. The density distribution of the gases on the MOFs were calculated using the fixed pressure task mode of Sorption module under 298K and 100 kPa (CH_4 fugacity: 99.78 kPa; C_2H_6 fugacity: 99.17 kPa; C_3H_8 fugacity: 98.36 kPa). The frameworks were assumed as rigid. DREIDING force field was used and the parameters of Zr are adopted from Universal force field. A total of 1×10^6 equilibration steps and 1×10^7 production steps were set. The van der Waals interactions were calculated by the atom-based method with a fine cutoff distance of

18.5 Å, whereas the Coulombic interactions were summed by the Ewald and group method.

The primary binding site and simulated isosteric heat (Q_{st}) values were calculated using the Adsorption Locator module. All the sets are similar to the sorption calculations.

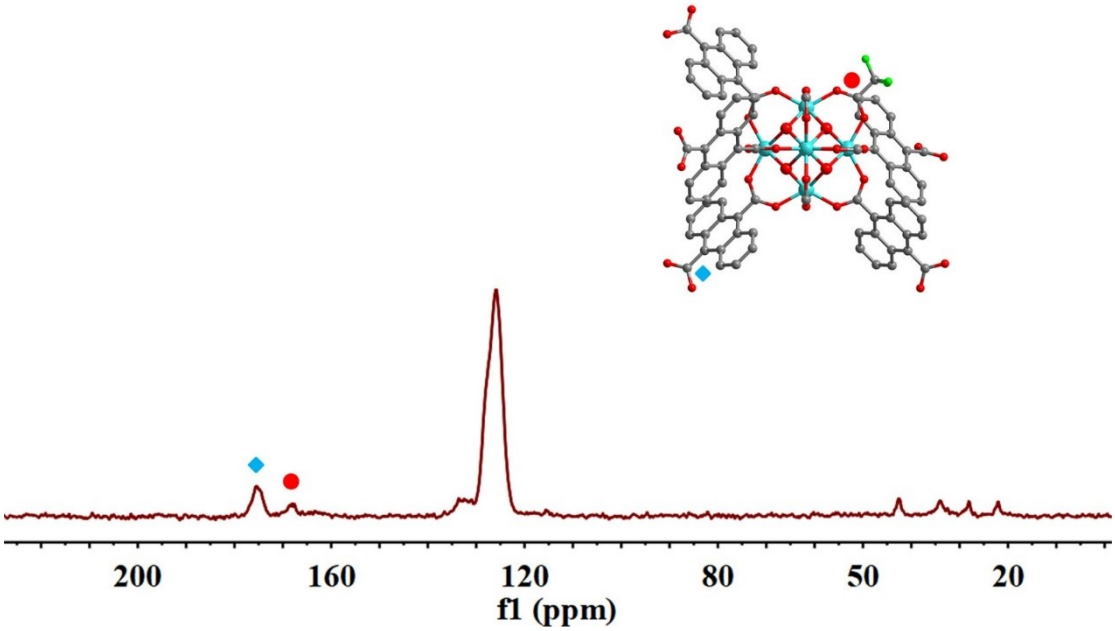

Figure S44. The solid-state ^{13}C NMR spectrum of UiO-66-Anth.

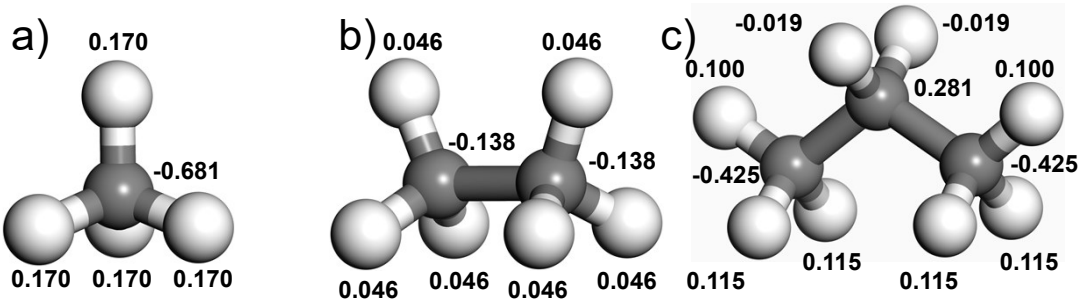

Figure S45. The ESP charges of a) CH_4, b) C_2H_6 and c) C_3H_8.

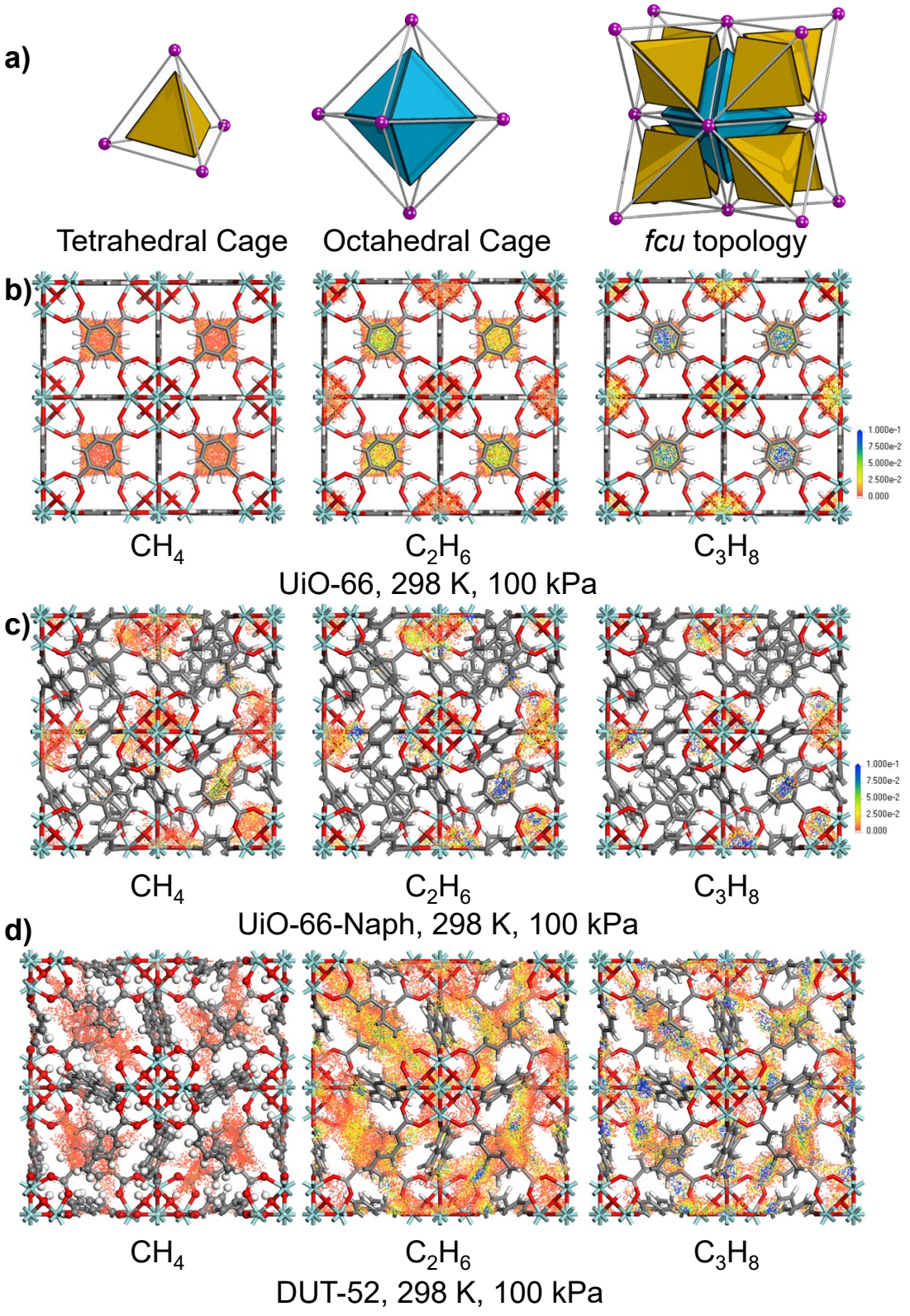

Figure S46. a) The pore structure and topology of UiO-66s. Density distribution of $CH_4/C_2H_6/C_3H_8$ in b) UiO-66, c) UiO-66-Naph and d) DUT-52 under 298K and 100 kPa, respectively.

Table S5. The simulated adsorption capacities (100 kPa), experimental adsorption capacities (100 kPa), calculated Q_{st} at primary adsorption site and experimental Q_{st} at zero coverage of UiO-66, UiO-66-Naph and DUT-52 for $CH_4/C_2H_6/C_3H_8$ adsorption.

MOF	Gas	Simulated adsorption capacities at 100 kPa ($cm^3\ g^{-1}$)	Experimental adsorption capacities at 100 kPa ($cm^3\ g^{-1}$)	Simulated Q_{st} ($kJ\ mol^{-1}$)	Experimental Q_{st} ($kJ\ mol^{-1}$)
UiO-66	CH_4	13.72	9.64	18.9	-
	C_2H_6	36.13	50.15	23.5	26.8
	C_3H_8	39.37	78.87	43	34.3
UiO-66-Naph	CH_4	13.43	6.01	23.5	-
	C_2H_6	34.16	37.30	33.2	29.5
	C_3H_8	28.31	61.15	44.6	37.9
DUT-52	CH_4	11.85	8.58	16.8	-
	C_2H_6	72.54	56.84	26.7	24.6
	C_3H_8	104.46	97.09	32.8	28.9

S9. References

1. S. N. Talapaneni, D. Kim, G. Barin, O. Buyukcakir, S. H. Je and A. Coskun, *Chem. Mater.*, 2016, **28**, 4460-4466.
2. J. Yan, B. Zhang and Z. Wang, *ACS Applied Materials & Interfaces*, 2018, **10**, 26618-26627.
3. J. Yan, B. Zhang, L. Guo and Z. Wang, *J. Phys. Chem. C*, 2019, **123**, 575-583.
4. C. Wang, J. Zhang and Z. Wang, *ACS Appl. Nano Mater.*, 2021, **4**, 14060-14068.
5. G. Li, C. Wang and Z. Wang, *Chem. Eng. J.*, 2022, **427**, 131985.
6. Z. Chen, K. Adil, Ł. J. Weseliński, Y. Belmabkhout and M. Eddaoudi, *J. Mater. Chem. A*, 2015, **3**, 6276-6281.
7. D. Wang, T. Zhao, Y. Cao, S. Yao, G. Li, Q. Huo and Y. Liu, *Chemical Communications*, 2014, **50**, 8648-8650.
8. H. Ma, H. Ren, S. Meng, F. Sun and G. Zhu, *Sci. Rep-UK.*, 2013, **3**, 2611.
9. J. Du, Y. Liu, R. Krishna, Y. Yu, Y. Cui, S. Wang, Y. Liu, X. Song and Z. Liang, *ACS Appl. Mater. Inter.*, 2018, **10**, 26678-26686.
10. J. Wang, R. Krishna, T. Yang and S. Deng, *J. Mater. Chem. A*, 2016, **4**, 13957-13966.
11. Y. Ye, J. Du, L. Sun, Y. Liu, S. Wang, X. Song and Z. Liang, *Dalton*

Transactions, 2020, **49**, 1135-1142.
12. Y. Xiong, T. Yang, S. Chen, C.-H. Zhang, C.-X. Chen, Z.-W. Wei, D. Wang, J.-J. Jiang and C.-Y. Su, *Crystal Growth & Design*, 2019, **19**, 300-304.
13. S. Meng, H. Ma, L. Jiang, H. Ren and G. Zhu, *J. Mater. Chem. A*, 2014, **2**, 14536-14541.
14. P. Zhang, X. Wen, L. Wang, Y. Zhong, Y. Su, Y. Zhang, J. Wang, J. Yang, Z. Zeng and S. Deng, *Chemical Engineering Journal*, 2020, **381**, 122731.
15. Y. Zhang, L. Yang, L. Wang, S. Duttwyler and H. Xing, *Angewandte Chemie International Edition*, 2019, **58**, 8145-8150.
16. L. Li, X. Wang, J. Liang, Y. Huang, H. Li, Z. Lin and R. Cao, *ACS Applied Materials & Interfaces*, 2016, **8**, 9777-9781.
17. P. Huang, C. Chen, F. Jiang, M. Wu and M. Hong, *Crystal Growth & Design*, 2019, **19**, 3103-3108.
18. J. Luo, J. Wang, Y. Cao, S. Yao, L. Zhang, Q. Huo and Y. Liu, *Inorganic Chemistry Frontiers*, 2017, **4**, 139-143.
19. J. Li, X. Luo, N. Zhao, L. Zhang, Q. Huo and Y. Liu, *Inorganic Chemistry*, 2019, **58**, 11269-11269.
20. J. Jia, L. Wang, F. Sun, X. Jing, Z. Bian, L. Gao, R. Krishna and G. Zhu, *Chemistry – A European Journal*, 2014, **20**, 9073-9080.
21. M. C. Das, H. Xu, S. Xiang, Z. Zhang, H. D. Arman, G. Qian and B. Chen, *Chemistry – A European Journal*, 2011, **17**, 7817-7822.
22. S. Gao, C. G. Morris, Z. Lu, Y. Yan, H. G. W. Godfrey, C. Murray, C. C. Tang, K. M. Thomas, S. Yang and M. Schröder, *Chemistry of Materials*, 2016, **28**, 2331-2340.
23. Y. Chen, Z. Qiao, D. Lv, H. Wu, R. Shi, Q. Xia, H. Wang, J. Zhou and Z. Li, *Industrial & Engineering Chemistry Research*, 2017, **56**, 4488-4495.
24. B. Yuan, X. Wang, X. Zhou, J. Xiao and Z. Li, *Chemical Engineering Journal*, 2019, **355**, 679-686.
25. L.-Z. Qin, X.-H. Xiong, S.-H. Wang, L. Zhang, L.-L. Meng, L. Yan, Y.-N. Fan, T.-A. Yan, D.-H. Liu, Z.-W. Wei and C.-Y. Su, *ACS Applied Materials & Interfaces*, 2022, **14**, 45444-45450.
26. W. Liang, H. Xiao, D. Lv, J. Xiao and Z. Li, *Separation and Purification Technology*, 2018, **190**, 60-67.
27. B. L. Newalkar, N. V. Choudary, P. Kumar, S. Komarneni and T. S. G. Bhat, *Chemistry of Materials*, 2002, **14**, 304-309.
28. Y. Ye, S. Xian, H. Cui, K. Tan, L. Gong, B. Liang, T. Pham, H. Pandey, R. Krishna, P. C. Lan, K. A. Forrest, B. Space, T. Thonhauser, J. Li and S. Ma, *J. Am. Chem. Soc.*, 2022, **144**, 1681-1689.
29. Q. Ding, Z. Zhang, C. Yu, P. Zhang, J. Wang, X. Cui, C.-H. He, S. Deng and H. Xing, *Sci. Adv.*, **6**, eaaz4322.
30. R. Krishna, *RSC Adv.*, 2017, **7**, 35724-35737.
31. R. Krishna, *ACS Omega*, 2020, **5**, 16987-17004.
32. Accelrys Materials Studio Release Motes, Release 5.5.1; Accelrys Software, Inc., San Diego, 2010.

33. L. Valenzano, B. Civalleri, S. Chavan, S. Bordiga, M. H. Nilsen, S. Jakobsen, K. P. Lillerud and C. Lamberti, *Chem. Mater.*, 2011, **23**, 1700-1718.
34. L. Gong, Y. Ye, Y. Liu, Y. Li, Z. Bao, S. Xiang, Z. Zhang and B. Chen, *ACS Appl. Mater. Inter.*, 2022, **14**, 19623-19628.
35. M. Fischer, F. Hoffmann and M. Fröba, *ChemPhysChem*, 2010, **11**, 2220-2229.